


Inductive and Capacitive Hysteresis of Current-Voltage Curves: Unified Structural Dynamics in Solar Energy Devices, Memristors, Ionic Transistors, and Bioelectronics

Juan Bisquert *

Institute of Advanced Materials (INAM), Universitat Jaume I, 12006 Castelló, Spain

 (Received 25 August 2023; revised 29 November 2023; published 8 January 2024)

Hysteresis observed in the current-voltage curves of both electronic and ionic devices is a phenomenon where the curve's shape is altered on the basis of the measurement speed. This effect is driven by internal processes that introduce a time delay in the response to an external stimulus, leading to measurements being dependent on the history of the past disturbances. This hysteresis effect has posed challenges, particularly in solution-processed photovoltaic devices such as halide perovskite solar cells, where it significantly complicates the evaluation of performance quality. In other devices, such as memristors and organic electrochemical transistors for neuromorphic applications, hysteresis is an inherent aspect of their functionality, facilitating transitions between different conductivity states. Natural and artificial ionically conducting channels also exhibit pronounced hysteresis, a crucial component for generating action potentials in neurons. In this study, we aim to categorize various forms of hysteresis by identifying shared elements among diverse physical, chemical, and biological conducting systems. Our method involves examining hysteresis from multiple angles, using simplified models that capture essential response types. We analyze system behavior using techniques such as linear sweep voltammetry and impedance spectroscopy and transient currents resulting from small voltage steps. Our investigation reveals two primary hysteresis types based on how current responds to rapid sweep rates: capacitive hysteresis and inductive hysteresis. These terms correspond to the dominant component in the equivalent circuit, determining the transient time response. Remarkably, these concepts provide insights into vastly different systems, spanning solar cells, capacitors, transistors, electrofluidic nanopores, and protein ion channels. The consistency in electrical responses across the different cases enables the identification of the primary cause of hysteresis. We also elucidate the frequency dependence of hysteresis and the stepwise responses of solar cells, illustrating how fundamental relaxations contribute to the overall surplus or deficit of current during extensive voltage sweeps that define the current-voltage curve.

DOI: [10.1103/PRXEnergy.3.011001](https://doi.org/10.1103/PRXEnergy.3.011001)

I. INTRODUCTION

Hysteresis in current-voltage curves is a phenomenon observed in various electronic, ionic, and molecular devices, significantly influencing their operational traits [1–9]. This effect leads to the current-voltage curve's behavior being contingent on the kinetic properties of the measurement process. This manifestation arises from a delay in the current response relative to voltage changes, thereby altering the steady-state current-voltage relationship during time-varying perturbations [10].

The main approach to hysteresis is obtained in the voltage sweep technique with scan velocity v_s used to measure the current-voltage curve. The voltage u varies with time as

$$u = v_s t. \quad (1)$$

The measurement is performed in a cycle of forward and reverse directions, or vice versa, so as to return to the starting state, and it may be repeated many times to check the stability of the response. This method is applied in many kinds of devices to obtain the current-voltage curve at a low sweep velocity and to provide the dynamic response by measuring at increasing sweep rates.

In general, hysteresis indicates that those physical phenomena that produce the current take some time to respond to the changes of applied voltage; hence, the current response depends on the history of the perturbation. Therefore one can apply, for example, a sinusoidal voltage covering the range $(-u_1, u_1)$, i.e., $u = u_1 \sin(\Omega_s t)$, instead

*bisquert@uji.es

Published by the American Physical Society under the terms of the [Creative Commons Attribution 4.0 International](https://creativecommons.org/licenses/by/4.0/) license. Further distribution of this work must maintain attribution to the author(s) and the published article's title, journal citation, and DOI.

of Eq. (1), and the hysteresis will be manifest as well. These measurements extend over a wide voltage window in highly nonlinear systems and typically the response is difficult to interpret in terms of the internal processes.

The specific physical mechanisms of hysteresis are analyzed in different research fields [1–7,9]. However, the related studies are not able to reveal the general principles of hysteresis that occurs across a wide variety of conducting systems, from photovoltaics to biology. Recent findings obtained in a variety of systems that shows intense hysteresis, such as in memristors and halide perovskite solar cells [11–16], enable us to provide a general classification of the main hysteresis types, using very simple models. As the phenomena that lie behind the hysteresis respond in different types of measurement of a time-dependent perturbation, this gives us an opportunity to probe the system in different ways to correlate the responses and obtain insight into the dominant phenomena. This is the approach we use in this work, in contrast to elaborating a mechanistic model for each separate physical system.

The advantage of this approach is that it combines the measurements of different experimental techniques, as the voltage scan over a wide window, impedance spectroscopy on a set of stationary states, the transient response to a set of step perturbations, and the frequency dependence of the current-voltage curves. By merging these methods on the basis of simple models that contain just a few parameters, one can obtain much insight into the dynamical properties of a system and one can predict and study important types of behavior. Of course, these methods can be also regarded as a first step towards elaborated molecular or transport models that implement particular mechanisms, sometimes using large parameter sets [12,17–21]. These more complex models must finally obey the general rules that will be outlined here.

We start by reviewing some specific systems of interest to see what general properties we can infer from observations of hysteresis. Since very different systems spanning biological and artificial ion channels, perovskite solar cells, memristors, and electrochemical transistors show properties that appear closely related, there must be an underlying structure to hysteresis effects. We establish such structure by analyzing the underlying equivalent circuit in the frequency domain [10,22]. We show that this approach provides a strong tool for the analysis of rather involved hysteresis features in a variety of experimental systems.

II. SOME EXAMPLES OF HYSTERESIS RESPONSE

Hysteresis has been a prominent phenomenon in lead halide perovskite solar cells, and its significance has been widely recognized [1–3,22–26]. In photovoltaic devices, hysteresis as shown in Fig. 1(A) is a major problem

that complicates the achievement of a stationary current-voltage curve, which is essential to determine the power conversion efficiency (PCE). This drawback makes it necessary to apply time-consuming advanced measurement protocols such as maximum power point tracking [30–35]. However, in other devices, such as memristors, as shown in Fig. 1(B) [27], the hysteresis loop is an intrinsic phenomenon providing a functionality that needs to be optimized. Indeed, the defining property of memristors [36–43] is the resistive switching from a low-resistance state to a high-resistance state in a *set* process that occurs at some threshold voltage. The low-resistance state is maintained in the return part of the cycle, and a *reset* process in the negative voltage side recovers the initial high resistance. Also, in field-effect transistors and in ionic transistors for memories, synapses, and neurons [44–48], the hysteresis is a main functional property.

Capacitors and electrochemical supercapacitors are central devices for electronics and energy storage. While they do not conduct direct current, they show hysteresis under voltage cycling, as presented in Fig. 1(C), which also shows a general characteristic of hysteresis in current-voltage curves: the effect becomes amplified when the voltage scan velocity increases.

The previous three systems have in common the property that the electrical current is electronic, although it is strongly influenced by ionic phenomena. Halide perovskites are mixed ionic-electronic conductors, where the slow hysteresis response is attributed to ionic reorganization in the sample [49–52]. In memristors, the resistive transition is associated with the buildup of an ionic filament [53,54]. The capacitive response in Fig. 1(C) is due to the ionic-electronic double layer of a metal plate in contact with a solution [28].

Hysteresis can be found also in many systems that have exclusively ionic conduction, such as ionically conducting glasses [4] and electrokinetic transport in nanopipettes [5]. Ionic current rectification is a frequently observed occurrence in both protein ion channels that form naturally and synthetic nanopores [55]. These phenomena are amply studied because transport through biological channels and pores plays a central role in many physiological processes in living organisms [56]. Inwardly rectifying potassium (KIR) channels in cell membranes control the passive and active electrical properties of cells, and they also link cellular metabolic state and membrane excitability *in vivo*. These channels operate by intracellular divalent cations and other molecules blocking the asymmetric open channel pores [57]. Figure 1(D) shows the hysteresis in the property of inward rectification of the KIR channel at different potassium concentrations [29]. The steady-state measurement produces a much larger current than the fast measurement. This is another way to look at hysteresis: to compare the current between a very slow measurement and a very fast one. The hysteresis of ion channels in the

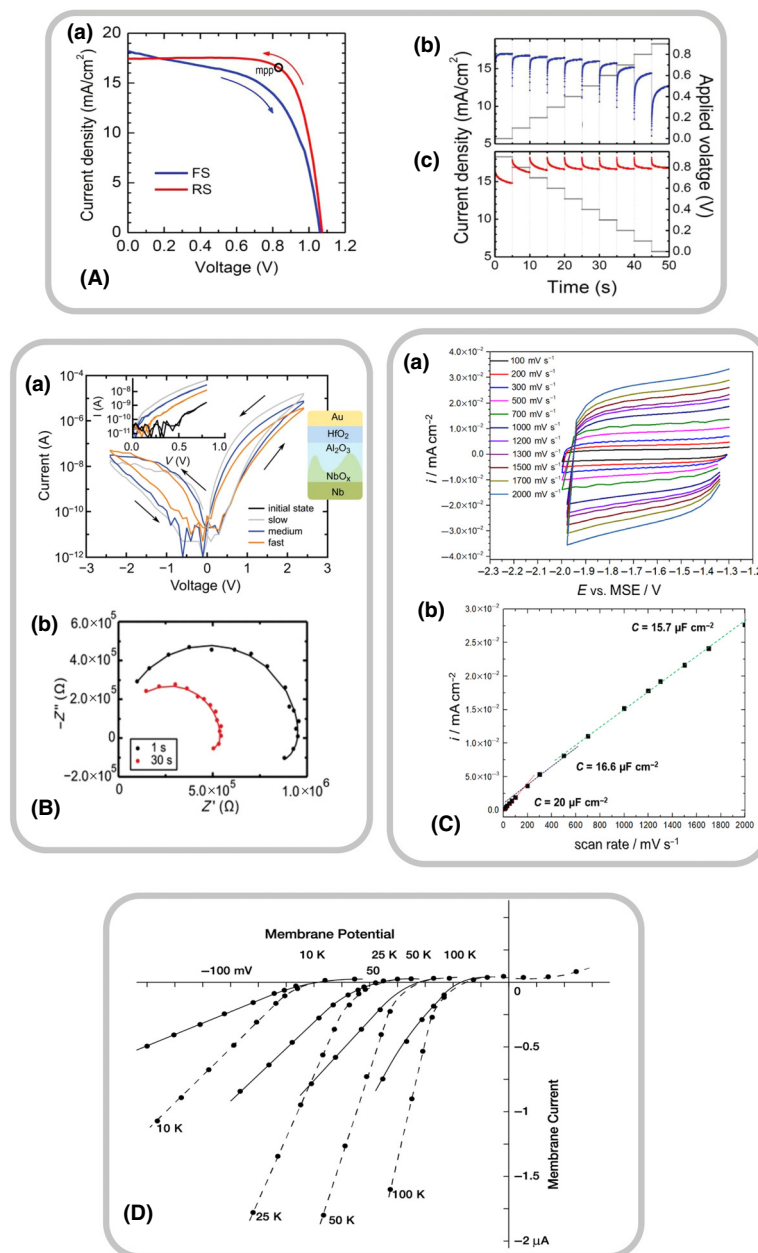


FIG. 1. (A) (a) I - V curves measured in forward scan (FS) and reverse scan (RS) for a perovskite solar cell using $\text{CH}_3\text{NH}_3\text{PbI}_3$. The maximum power point (mpp) is indicated. The voltage settling time was 200 ms and the light intensity was AM1.5 G 1 sun (100 mW cm^{-2}). (b),(c) Time-dependent photocurrent response as a function of voltage settling time in (b) forward scan and (c) reverse scan. Reproduced with permission from H.-S. Kim, N.-G. Park, *J. Phys. Chem. Lett.* 5, 2927–2934 (2014). Licensed under a Creative Commons Attribution (CC BY 4.0) license. (B) (a) Characteristic current-voltage curves of a hafnium oxide-based memristive device switching from the high-resistance state to the low-resistance state and back. Voltage ramps at three different speeds: gray, slow (43.6 mV s^{-1}); blue, medium (480 mV s^{-1}); orange, fast (4.8 V s^{-1}). The inset shows readout I - V characteristics of different resistance states depending on the ramp speed of the switching. A sketch of the layer stack of the memristive device is given on the right side. (b) Complex plane impedance plots after application of 2.1 V for 1 and 30 s. Reproduced with permission from R. Marquardt, F. Zahari, J. Carstensen, G. Popkirov, O. Gronenberg, G. Kolhatkar, H. Kohlstedt, M. Ziegler, *Adv. Electron. Mater.* 9, 2201227 (2023). Licensed under a Creative Commons Attribution (CC BY 4.0) license. (C) (a) Experimental cyclic voltammetry curves of an Al electrode in $0.01 \text{ M Na}_2\text{SO}_4$ recorded at scan rates between 100 and 2000 mV s^{-1} and (b) the capacitive current as a function of the scan rate. Reproduced with permission from O. Gharbi, M. T. T. Tran, B. Tribollet, M. Turmine, V. Vivier, *Electrochim. Acta* 343, 136109 (2020). Copyright 2020, Elsevier. (D) Current-voltage relations of the egg cell membrane at four different K concentrations (10, 25, 50, and 100 mM) in Na-free medium. Continuous lines, instantaneous current; broken lines, steady-state current. Reproduced with permission from S. Hagiwara, S. Miyazaki, N. P. Rosenthal, *J. Gen. Physiol.* 67, 621–638 (1976). Copyright 1976, Rockefeller University Press.

cell membrane is a central property of neuron functionality. In the model of Hodgkin and Huxley for the dynamics of action potentials in neurons [58,59], the concerted delay of the sodium and potassium channels that conduct opposite currents is responsible for the production of the action potentials by which neurons transmit information.

Artificial solid-state nanopores and nanochannels can be regarded as mimics of protein ion channels and have also been developed for sensing applications. The underlying physical cause of rectification arises from the asymmetry in the geometry of the nanopore and/or the distribution of surface charges and their polarities along the sidewalls of the nanopore [55]. Conical nanopores are observed to display hysteresis by decreasing current at higher scan rates [5,60–62].

III. DISTINCTION BETWEEN CAPACITIVE AND INDUCTIVE RESPONSE

We briefly analyze the physical nature of hysteresis. In the examples in Fig. 1 we can observe two different kinds of hysteresis behavior with respect to the velocity of the external perturbation. In the capacitor corresponding to Fig. 1(C) the current increases with the scan rate. The square shape becomes progressively larger. However, in the ionic channel corresponding to Fig. 1(D) the fastest scan rates produce a decreasing slope and lower total current, as found also in conical nanopores [5,60–62].

As we are concerned with the current-voltage curve, the ac impedance provides a natural framework to analyze the response. In general, a physical model of any kind of device is highly nonlinear. However, operating at a stationary point of the current-voltage curve, one can perform a small signal measurement at angular frequency ω of the voltage-current ratio, and this is called the “impedance” Z . Then an arbitrary complex physical system becomes a linear model that can be represented in terms of resistances, capacitors, and inductors [63–65]. This method also serves to analyze stability and other significant properties of the nonlinear system [66–69]. In halide perovskite solar cells, the connection between the impedance components and the hysteresis behavior is understood [10,25,51,70,71], with important application for stabilization of the current-voltage curves and determining the stationary performance [72].

One needs to keep in mind that the elements of the equivalent circuit depend strongly on the stationary voltage, so nonlinear properties, as the hysteresis behavior, may change along the measured current-voltage curve. This feature is commented on in Sec. VII.

The constitutive equation of a constant capacitor of capacitance C is the charge Q to voltage V relation

$$Q = CV. \quad (2)$$

The current under voltage sweep (1) is given by

$$I = \frac{dQ}{dt} = Cv_s. \quad (3)$$

Thus, the forward current is positive and the reverse current is negative; see Fig. 1(C)(a). In each case the current is proportional to the scan rate. This fact is well known and it is widely used for the characterization of electrochemical capacitors, as shown in Fig. 1(C)(b) [28].

The impedance of the capacitor is obtained by the Laplace transform of Eqs. (2) and (3), and the result is

$$Z = \frac{1}{i\omega C}. \quad (4)$$

Now consider an inductor with inductance L , which is described by the equation

$$V = L \frac{dI}{dt}, \quad (5)$$

with the correspondent impedance

$$Z = i\omega L. \quad (6)$$

On the basis of Eq. (4) we can define a generalized complex capacitance C^* as follows:

$$C^* = \frac{1}{i\omega Z}. \quad (7)$$

We obtain the capacitance of the inductor as [73]

$$C^* = -\frac{1}{\omega^2 L}. \quad (8)$$

Therefore, the inductor element is associated with a “negative capacitance” [74,75].

We observe that a capacitor and an inductor provide very different impedance responses, due to their intrinsically different time delays. Next we analyze the significance of these properties for the interpretation of hysteresis.

IV. LINEAR MODEL WITH MEMORY TO EXPLAIN THE BASIC TYPES OF HYSTERESIS

As mentioned, ionic-electronic devices may require very complex models, providing intricate hysteresis properties. However, there is an intrinsic structure to many models that we can analyze on the basis of a simple model with two equations that link the current, I_{tot} , the voltage, u , and an additional internal state variable, w . To explore these basic

properties of hysteresis, we consider the linear equations

$$I_{\text{tot}} = \frac{u}{R_b} + w + C_m \frac{du}{dt}, \quad (9)$$

$$\tau_k \frac{dw}{dt} = \frac{u}{R_w} - \frac{w}{b}, \quad (10)$$

where C_m is a capacitance, and R_b and R_w are constant resistances. The total current in Eq. (9) has three components: an instantaneous current u/R_b , a capacitive current, and a slow variable current w that is determined by the relaxation equation (10), with constants τ_k and b .

We calculate the impedance spectroscopy response of this model for a small sinusoidal perturbation of angular frequency ω . Since Eqs. (9) and (10) form a linear system, the Laplace transform for the variable $s = i\omega$ is

$$\hat{I}_{\text{tot}} = \frac{\hat{u}}{R_b} + w + C_m s \hat{u}, \quad (11)$$

$$\tau_k s \hat{w} = \frac{\hat{u}}{R_w} - \frac{\hat{w}}{b}. \quad (12)$$

Here the circumflex accent indicates a small perturbation of the variable y . We obtain the impedance as follows:

$$Z(s) = \frac{\hat{u}}{\hat{I}_{\text{tot}}} = \left[C_m s + R_b^{-1} + \frac{1}{R_a + L_a s} \right]^{-1}, \quad (13)$$

where the resistance and the inductor are defined as

$$R_a = \frac{R_w}{b}, \quad (14)$$

$$L_a = R_w \tau_k, \quad (15)$$

and the inductor characteristic time is given by

$$\tau_L = \frac{L_a}{R_a} = b \tau_k. \quad (16)$$

The equivalent circuit that represents Eq. (13) is shown in Fig. 2(a). This model indicates the three parallel branches mentioned before: the capacitive charging, the direct conduction mode R_b , and the slow inductive branch (R_a, L_a). The capacitive element has been included in Eq. (9), as most devices do have an intrinsic capacitance. On the other hand, the inductive element is due to the delay equation (10) for the slow variable. This is not a general property of devices, but it is more common that one may suspect, especially when ionic-electronic mixed effects are present. Since the inductor is not based on electromagnetism, it is generally described as a chemical inductor [73,76].

When the inductor effect is negligible, the impedance is formed by a positive $R_b C_m$ arc; see Fig. 2(b), arc *A*. If, however, the inductor parameter is large, the impedance traces

a loop in the fourth quadrant that represents a “negative capacitance” feature, as shown by arc *B* in Fig. 2(b).

Figure 2(e) shows a more general equivalent circuit [77] with an $R_a C_a$ line that produces a double-arc feature at low frequencies that will be discussed later. This feature, corresponding to surface polarization of ion diffusion that is blocked at the contacts, was originally observed in perovskite solar cells by light-modulated techniques [78] and by impedance methods [79,80].

In the following we argue that the combination of the standard $R_b C_m$ indicated in Fig. 2(a) with the delay mode represented by the $R_a L_a$ branch explains the existence of both types of hysteresis mentioned earlier in current-voltage curves of electronic devices as capacitors and memristors, and the two types will be classified as capacitive and inductive hysteresis [11–16,81,82].

The stationary current-voltage characteristic of the model is given by

$$I_{\text{dc}} = \left(\frac{1}{R_b} + \frac{1}{R_a} \right) u \quad (17)$$

and the current will be modified when the voltage scan rate v_s is finite.

We now restrict the model to the time dependence in Eq. (1). We first discuss the case in which the slow current w responds without delay, to focus on the capacitive current; hence, $w = u/R_a$, and the total current is given by

$$I_{\text{tot}} = \frac{u}{R_b} + \frac{u}{R_a} + \Delta I_c, \quad (18)$$

where

$$\Delta I_c = C_m v_s. \quad (19)$$

As shown in Fig. 2(c), under a forward scan, a positive capacitive current is added to the stationary current. The capacitive current is proportional to the scan rate v_s , as already stated in Eq. (3).

We now discuss the second component of the time-dependent current, the slow variable w that responds to the applied voltage with characteristic time τ_k . From Eq. (10), we obtain for a constant sweep rate

$$\tau_k v_s \frac{dw}{du} = \frac{u}{R_w} - \frac{w}{b}. \quad (20)$$

This equation needs to be integrated and inserted into Eq. (9) to obtain the current. For the initial condition $w(0) = 0$, the solution is

$$I_{\text{tot}}(u) = \frac{u}{R_b} + \frac{u}{R_a} + \frac{v_s \tau_L}{R_a} (e^{-u/(v_s \tau_L)} - 1). \quad (21)$$

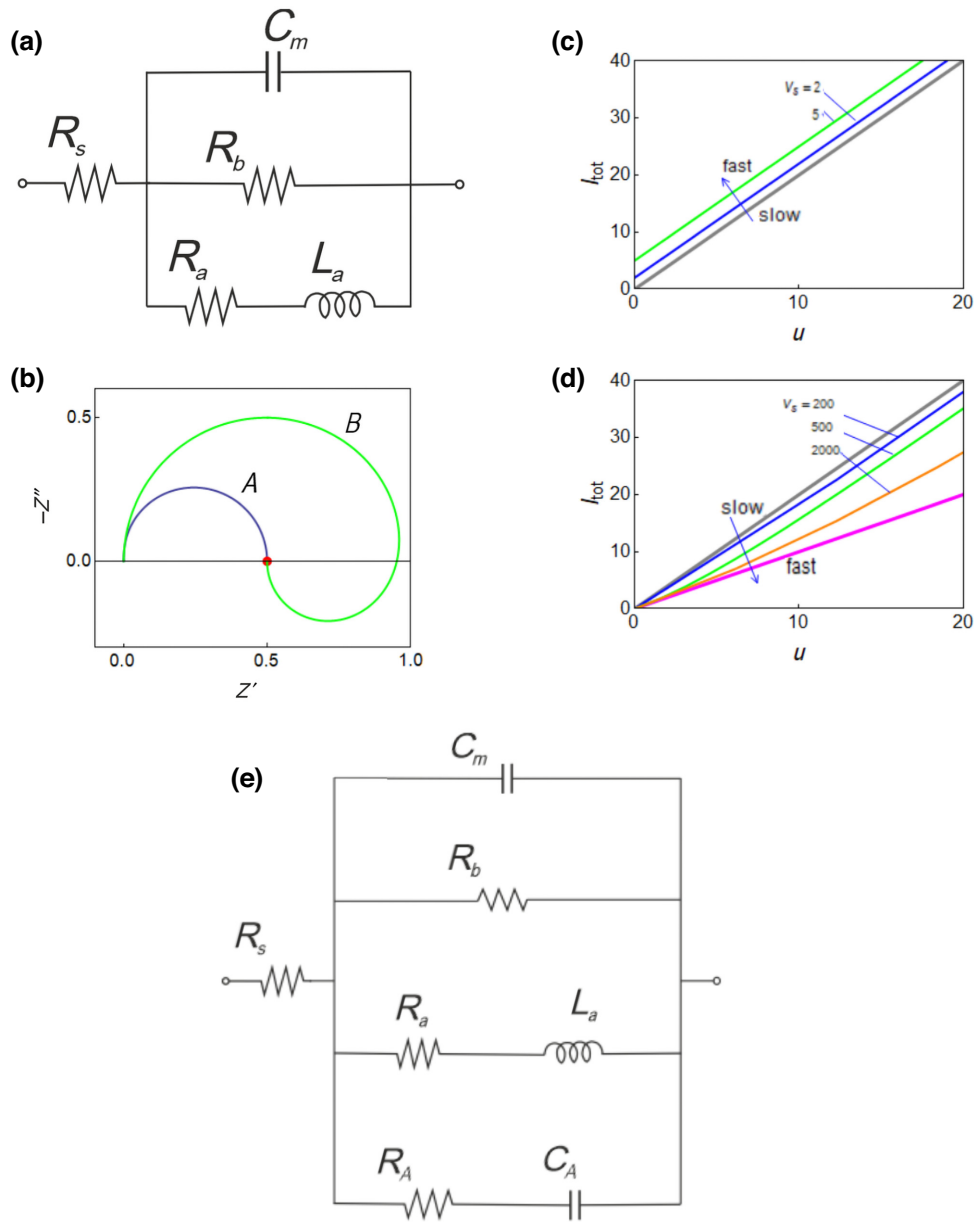


FIG. 2. (a) Equivalent circuit model. (b) Impedance spectra for $C_m = 1$, $R_b = 1$, $R_a = 1$, and $L_a = 0.1$ (arc A) or $L_a = 20$ (arc B). The red point is the dc resistance. (c),(d) Current-voltage curves at different voltage sweep rates v_s , $u = v_s t$. (c) The state variable responds fast, and the capacitive current with capacitance $C_m = 1$ is added to the direct current. The steady-state current (slow) is shown as the gray line. (d) The capacitance is removed, $C_m = 0$, and the variable w contributes to the current. The purple line corresponds to an infinitely fast scan. The parameters are $R_b = 1$, $R_a = 1$, $\tau_k = 0.01$, and $b = 1$. (e) A more general equivalent circuit model. The curves in (b), (c), (d) are given in arbitrary units to illustrate the general shapes caused by the indicated parameters.

The inductive current $\Delta I_L = I_{tot} - I_{dc}$ is negative in the forward scan and positive in the reverse scan, as shown in Fig. 2(d), corresponding to the negative capacitance of Eq. (8). If v_s is small, the full current in Eq. (17) is activated, indicated by the gray line in Fig. 2(d). However, if $v_s \tau_L \gg u$, the inductive current through R_a vanishes in Eq. (21) and the remaining fast component

$$I_{fast} = \frac{u}{R_b} \quad (22)$$

is indicated by the purple line in Fig. 2(d). This representation provides an excellent account of the properties of the KIR channel observed in Fig. 1(D).

V. GENERAL CHARACTERISTICS OF INDUCTIVE AND CAPACITIVE HYSTERESIS

To obtain a general system that displays both capacitive and inductive hysteresis, we can write the dynamical equations with the same general structure of Eqs. (9) and (10),

but with arbitrary nonlinear functions for conductivity, f , and time delay of the internal variable, g , corresponding to the specific physical situation:

$$I_{\text{tot}} = C_m \frac{du}{dt} + f(u, w), \quad (23)$$

$$\tau_k \frac{dw}{dt} = g(u, w). \quad (24)$$

The delay equation (24) is very typical of broad kinds of model, such as the Hodgkin-Huxley model in neurobiology [58,59], the related models for protein ion channels with memory effects [83,84], and the generic model of a memristor with an internal state variable [36,40]. It was reported in very old measurements that ion channels in neurons contain a large inductor component [85–87]. In the field of halide perovskite solar cells, this model represents the essential mechanism for the electronic recombination controlled by ionic motion that has been suggested in many papers to explain the negative capacitance observed in the device [15,21,79,88,89].

To determine the equivalent circuit, we obtain the small perturbation expansion:

$$\hat{I}_{\text{tot}} = C_m s \hat{u} + f_u \hat{u} + f_w \hat{w}, \quad (25)$$

$$\tau_k s \hat{w} = g_u \hat{u} + g_w \hat{w}, \quad (26)$$

where the subindex indicates a partial derivative, $f_u = \partial f / \partial u$ and so forth.

Equations (25) and (26) reproduce Eqs. (11) and (12) and the impedance model is the same as Eq. (13). The

equivalent circuit elements are given by [69,73,77]

$$R_b = \frac{1}{f_u}, \quad (27)$$

$$R_a = -\frac{g_w}{f_w g_u}, \quad (28)$$

$$L_a = \frac{\tau_k}{f_w g_u}. \quad (29)$$

These elements may all be functions of the voltage according to the properties of the functions f and g producing evolutions of the hysteresis properties that are discussed below.

The inductor time constant is given by

$$\tau_L = -\frac{\tau_k}{g_w}. \quad (30)$$

Consider the special role of the constant b in Eq. (10) and more generally g_w in Eq. (26) for the system's stable response. If $b < 0$ ($g_w > 0$), then the inductor time constant τ_L is negative, which produces an exponential growth in Eq. (24). Then the system is unstable [90]. Hence, we require that $g_w < 0$.

We can now generalize the results of Fig. 2 for a nonlinear system of the type of Eqs. (23) and (24). We apply a voltage schedule with varying sweep rates, as indicated in Fig. 3(a). In the first part we have $v_s > 0$ and in the second part we have $v_s < 0$, so as to return to the initial voltage. Similarly, the voltage can be cycled with frequency Ω_s .

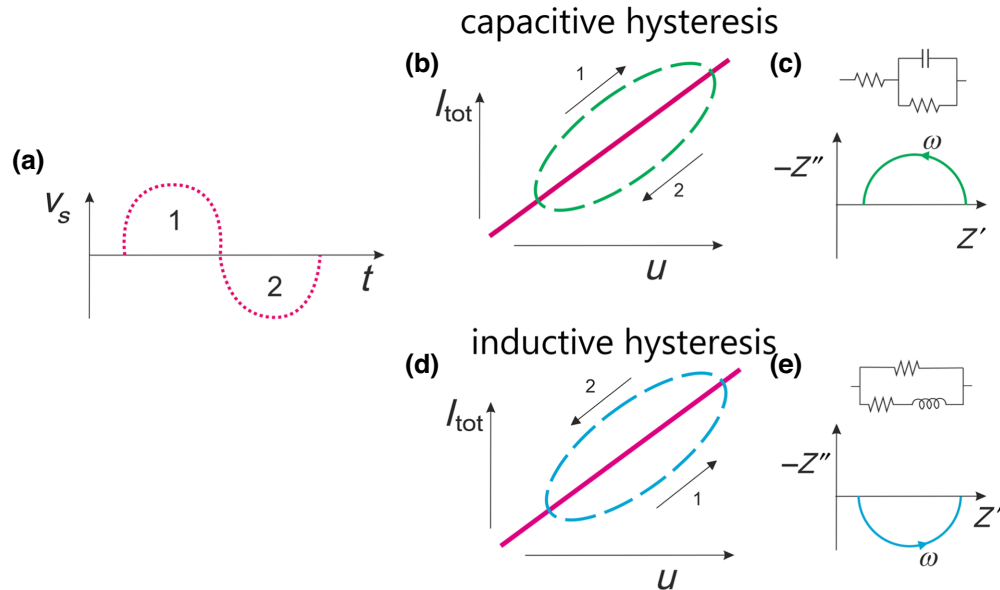


FIG. 3. (a) Time-varying voltage scan rate with a positive scan direction part (1) and a negative scan direction part (2) of the cycle. (b)–(d) Current-voltage curves. The thick line represents the stationary current and the dashed line represents the current under the varying speed indicated in (a). (c)–(e) Basic impedance spectra and the associated equivalent circuit. The arrow indicates the direction of increasing angular frequency. (b),(c) Capacitive system. (d),(e) Inductive system.

We assume first a system that is dominated by the capacitive transient current; see Fig. 3(b). In the first part of the cycle it is $\Delta I_c > 0$, while in the second part it is $\Delta I_c < 0$. Therefore, the current will describe a clockwise loop as indicated in Fig. 3(b). We term this loop a “capacitive hysteresis”, and the associated impedance spectrum is a positive arc; see Fig. 3(c).

If, on the other hand, the system is dominated by the slow current component, then we have $\Delta I_L < 0$ in the first part and $\Delta I_L > 0$ in the second part. The hysteresis loop is counterclockwise, and we term it “inductive hysteresis”; see Fig. 3(d). The correspondent impedance spectrum is a negative arc as indicated in Fig. 3(e).

From Fig. 3 we conclude that for a capacitive hysteresis the forward current is larger than the stationary curve, and the current in the reverse direction is lower. However, for solar cell devices, the representation is often reversed. This is because the total current is given by

$$I_{\text{tot}} = I_{\text{photo}} - I_{\text{rec}}, \quad (31)$$

where I_{photo} is the photocurrent, taken to be positive, and I_{rec} is the recombination current associated with Eq. (23), which contains the hysteresis effects. Hence, for the forward scan the capacitive hysteresis current appears lower than the reverse scan current, as shown in Fig. 1(A) [22], and the effect of capacitive and inductive hysteresis in the solar cell current is opposite that in Fig. 3. In the field of halide perovskite solar cells, the capacitive hysteresis is termed “regular” and the inductive hysteresis is termed “inverted” [12,18,26,91].

A major problem for determining the PCE in perovskite solar cells with hysteresis, mentioned long ago [1], is that the performance is different in the forward and return cycles, consequently necessitating equilibration methods by successive slow scans [34,72]. The PCE is a product of current and voltage at the maximum power point. We can see in Fig. 1(A) that the capacitive hysteresis produces a larger PCE in the reverse scan than in the forward cycle [22], while for inductive hysteresis the converse is true: the PCE is larger in the forward direction [10,12]. These properties are independent of the sign convention adopted to plot the current.

In the literature there are different ways to quantify the capacitive and inductive hysteresis. A hysteresis index is based on the integral of the hysteresis loop [8,92]:

$$A = \int_{V_1}^{V_2} IdV. \quad (32)$$

This or equivalent integrals (such as the hysteresis enrichment charge [5,62]) provide a positive area for inductive hysteresis and a negative area for a capacitive hysteresis, or vice versa, according to the sign convention for the current.

VI. INTERPRETATION OF SYSTEMS WITH CAPACITIVE AND INDUCTIVE HYSTERESIS

Starting from the reference linear system formed by Eqs. (9) and (10) we pass to the more general model of Eqs. (23) and (24) that produces a general connection between the dominant elements of impedance spectroscopy and the type of hysteresis loop that will be obtained [14,16]. Many materials and systems may require still additional features with respect to Eqs. (23) and (24), depending on the morphology, the number of internal processes, and their evolution with the applied voltage [11, 93]. Nevertheless, the basic distinction of capacitive and inductive hysteresis observation provides a useful diagnostic technique, as the equivalent circuit obtained from the measurement of small-perturbation impedance spectroscopy can tell us the dominant hysteresis type that is expected in the large perturbation of linear sweep voltammetry, according to the frequency or velocity of the measurement [13,15,22]. Furthermore, the observation of the prevalent type of hysteresis can produce a guideline for the basic structural equations needed in a specific model system.

To further determine the significance of these questions, in the following we provide a set of examples where the connection between hysteresis and impedance illustrates the kinetic and physical elements of the system.

First we return to the hafnium oxide–based memristor corresponding to Fig. 1(B) and we note that the large inductive (“inverted”) hysteresis loop characteristic of the set process of the memristor, in which the resistance switches to a high-conductance state [94], reveals the appearance of the associated inductor in the complex plane plot of the impedance, Fig. 1(B)(b), as predicted by the general model. Equations (23) and (24) are the standard constitutive equations of a memristor [36,40,95], and we can remark that memristors, in the voltage range of the set process, will display a large *inverted* hysteresis loop in the set cycle, where the current increases at a certain threshold of voltage or current [12–14]. The associated chemical inductor appears naturally in the impedance response, as observed in Fig. 1(B)(b). A similar connection of inverted hysteresis and the inductive loop has been reported for halide perovskite memristors and solar cells [14,16,96], and these devices are discussed in Sec. VII.

To further analyze the change of hysteresis type, we consider the properties of conical ionic channels in an electrolyte solution, shown in Fig. 4(a), that show rectifying properties due to the electrical interaction between the functionalized charges on the conical pore surface and the nanoconfined ionic solution [55,98]. Nanopore memristors have been studied for their strong hysteresis properties [5,61,62], and inductive impedance has been reported [60], but the correlation between the type of hysteresis and the inductive element was not established.

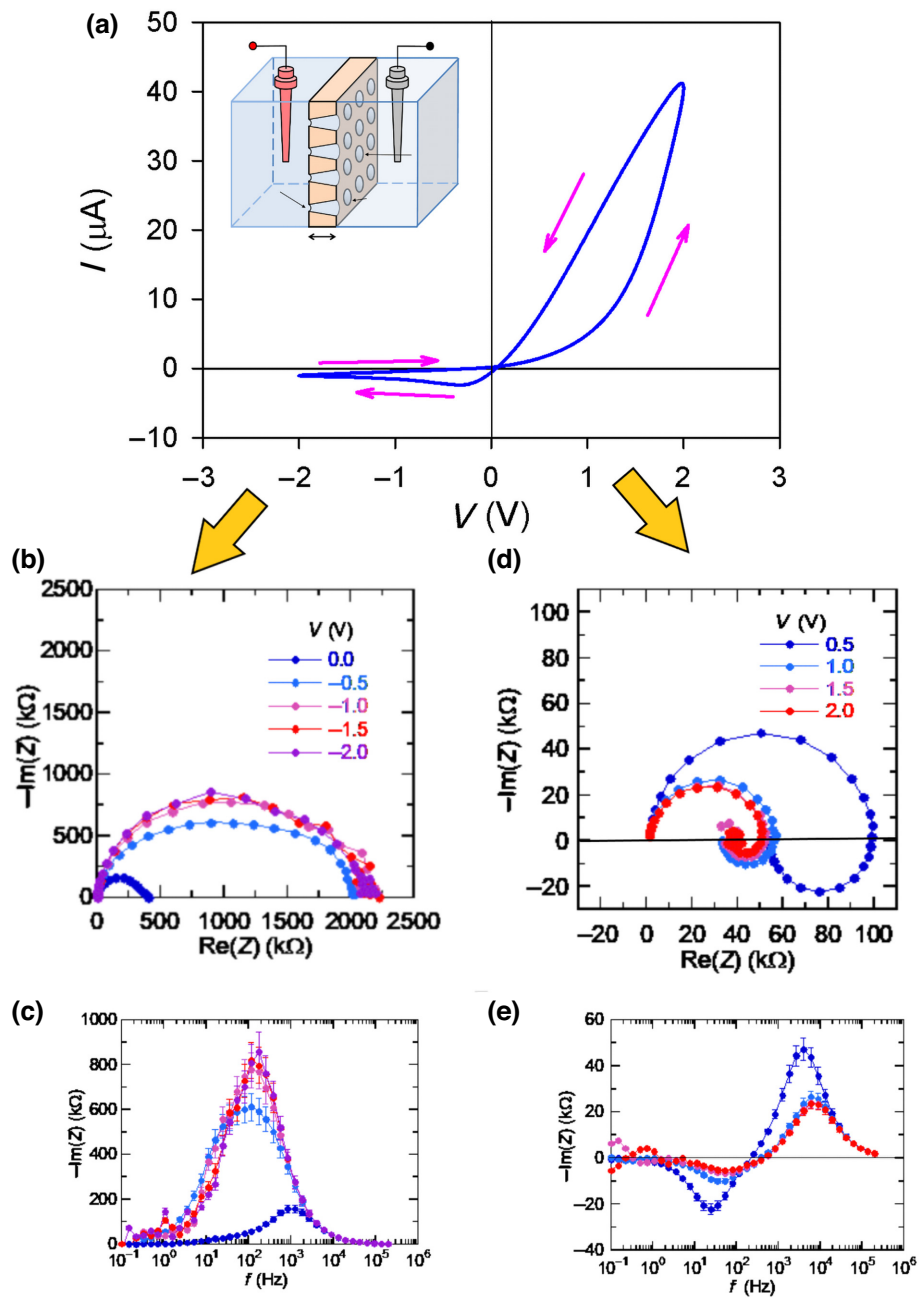


FIG. 4. (a) Current-voltage curve measured at frequency $\Omega_s = 10$ Hz for a multipore membrane in 100 mM KCl solution at neutral $p\text{H}$. The inset shows the electrochemical cell with the membrane. (b) Impedance spectra at different reverse voltages, with the corresponding Bode plot of the imaginary part of the impedance in (c). (d),(e) Impedance spectra and Bode plots at forward voltage. Adapted from P. Ramirez, J. Cervera, S. Nasir, M. Ali, W. Ensinger, S. Mafé, *J. Colloid Interface Sci.* 655, 876–885 (2024) with permission from Elsevier.

We show in Fig. 4 results obtained recently by Ramirez *et al.* [97]. On the positive voltage side of the current-voltage curve in Fig. 4(a), the memristive pores show a strong inverted hysteresis, accompanied by the notorious inductive impedance loop in Fig. 4(d). The forward and reverse scans of the current-voltage curve cross at the origin, and it follows that the type of hysteresis is changed.

On the negative side, the hysteresis is capacitive, and the impedance shows purely capacitive spectra; see Fig. 4(b).

Remarkably, it has been shown that the side of inductive hysteresis of the pore response can be transposed from a positive potential to a negative potential by modulation of the electrolyte composition [8], opening interesting applications for nanofluidic neuromorphic circuits.

Another system of current interest is organic electrochemical transistors for application in neuromorphic systems [43,45,46,99–101] and bioelectronics [48,102]. The channel of these three-terminal devices is formed by an organic mixed ionic-electronic conductor (OMIEC) [103]; see Fig. 5(a). The variations in the gate-source voltage u_g govern the flow of mobile ions between the OMIEC channel and the electrolyte. This modulation of ions leads

to changes in the doping states and the conductivity of the OMIEC channel. Hysteresis by a mismatch between the forward scan and the backward scan in the transfer curves has been amply reported [7,93,105,106], and it was attributed to a delay of the ion charging effect [107]. Hysteresis is also prevalent in field-effect transistors [6].

Recently, the following model to explain hysteresis in organic electrochemical transistors was proposed [104]:

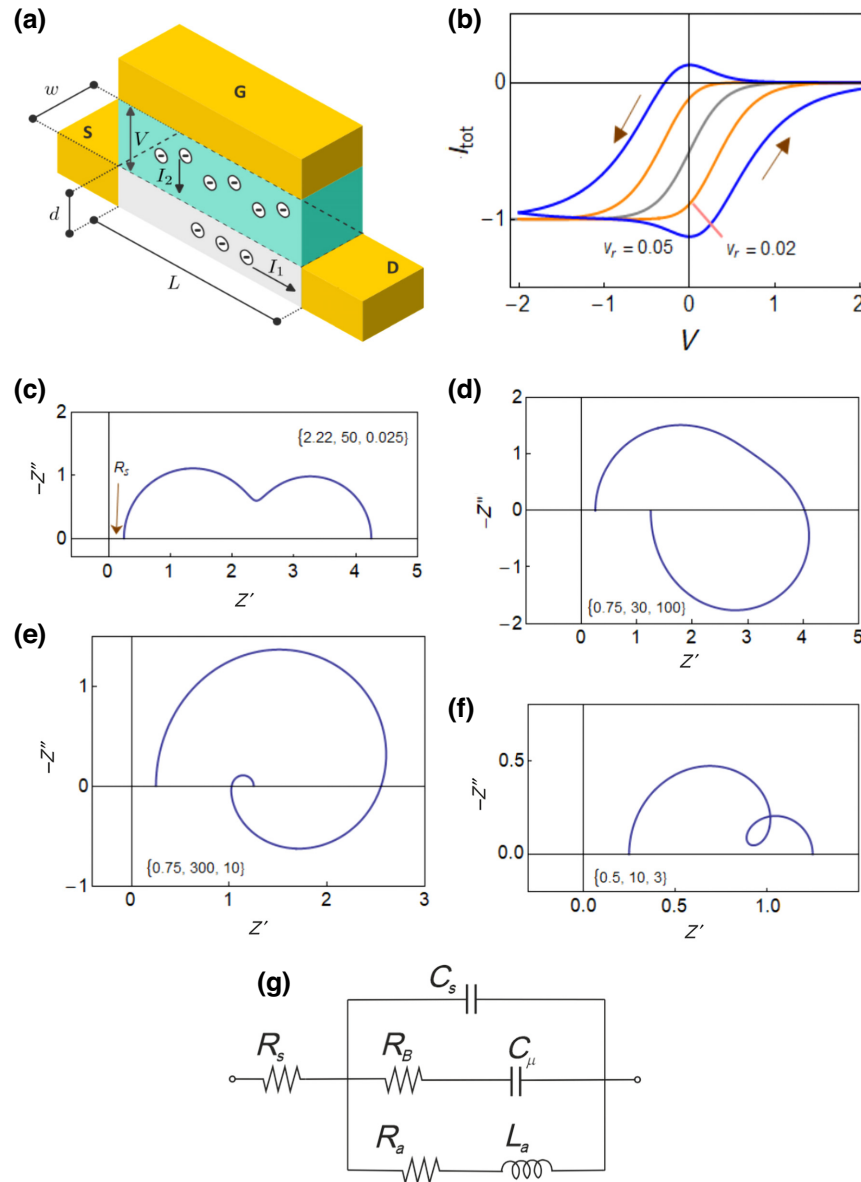


FIG. 5. (a) Operation of an organic electrochemical transistor and geometric dimensions. The green zone is the electrolyte, the gray zone is the OMIEC layer, and the yellow zones are the gate (G), source (S), and drain (D) electrodes. The anions inserted into the film are the source of electronic holes that carry the current. (b) Hysteresis in current-voltage curves due to the ion diffusion effect at different voltage sweep rates (v_r) and the equilibrium curve (gray). The parameters are as follows: $L = 10$, $d = 0.1$, $w = 1$, $X_0 = 100$, $u_0 = 0$, $V_m = 0.2$, $q\mu_p u_d = 1$, $R_s = 0.1$, $C_s = 1$, and $\tau_d = 100$. Impedance spectra for different sets of parameters: $R_s = 0.25$, $C_s = 1$, and (c) $R_a = 5$, $L_a = 0.1$, $R_B = 5$, and $C_\mu = 10$, (d) $R_a = 1$, $L_a = 10$, $R_B = 3$, and $C_\mu = 100$, (e) $R_a = 1$, $L_a = 100$, $R_B = 3$, and $C_\mu = 10$, and (f) $R_a = 1$, $L_a = 3$, $R_B = 1$, and $C_\mu = 10$. The indicated vectors are the time constants $(R_a^{-1} + R_B^{-1})^{-1} C_s$, $R_B C_\mu$, and L_a/R_a . (g) Equivalent circuit model. Adapted with permission from J. Bisquert, J. Phys. Chem. Lett. 14, 10951–10958 (2023). Licensed under a Creative Commons Attribution (CC BY 4.0) license.

$$I_{\text{tot}} = -B_d X - Q_v \frac{dX}{dt} + C_s \frac{du_g}{dt}, \quad (33)$$

$$\tau_d \frac{dX}{dt} = X_{\text{eq}} - X, \quad (34)$$

where the constants

$$B_d = \frac{wd}{L} q\mu_p u_d \quad (35)$$

and $Q_v = wLdq$ are defined in terms of the geometric features shown in Fig. 5(a), μ_p is the hole mobility, u_d is the channel voltage difference, and X is the variable ionic density in the channel that fixes the hole concentration as $p = X$ and modulates the conductivity.

In Eq. (33), the capacitance C_s is associated with the OMIEC surface capacitance. The term $B_d X$ is the drift current, and the term with dX/dt is the current caused by ion insertion in the film, according to the model of Bernards and Malliaras [108]. Equation (34) corresponds to ion diffusion in the film, up to the equilibrium function $X_{\text{eq}}(u_g)$. The insertion process is controlled by the characteristic diffusion time

$$\tau_d = \frac{d^2}{D_X}, \quad (36)$$

where D_X is the chemical diffusion coefficient of ions. We remark that the system formed by Eqs. (33) and (34) is of the type given by Eqs. (23) and (24) (with an additional feature of dX/dt that is further discussed later).

Figure 5(b) shows as a gray line the equilibrium current, $I_{\text{tot}} = -B_d X_{\text{eq}}$. When the voltage is swept at a constant rate, inductive hysteresis happens, Fig. 5(b), due to Eq. (34), as expected from our general model, and as observed experimentally [7].

The calculation of the impedance model from Eqs. (33) and (34) gives the equivalent circuit shown in Fig. 5(g). This is the model shown in Fig. 2(e) with the chemical inductor line due to Eq. (34). The impedance parameters are

$$C_\mu = -Q_v \frac{dX_{\text{eq}}}{du_g}, \quad (37)$$

$$R_a = \frac{L^2}{C_\mu \mu_p u_d}, \quad (38)$$

$$R_B = \frac{d^2}{C_\mu D_X}, \quad (39)$$

$$L_a = \frac{L^2 d^2}{C_\mu \mu_p u_d D_X}. \quad (40)$$

In contrast to Fig. 2(e), the equivalent circuit of the transistor does not have a direct R_b conductance. This is due to the different three-terminal configuration.

C_μ of Eq. (37), which we obtain from Fig. 5(g) in the line $R_B C_\mu$ [as in Fig. 2(e)], is the chemical capacitance of intercalated ions. It is defined by the derivative of the thermodynamical function with respect to the electrochemical potential [109,110]. R_B is a diffusion resistance for the vertical current of intercalation from the electrolyte towards the film interior. These two terms are generated by the derivative dX/dt . This is a new feature with respect to Eq. (23), first obtained in Ref. [79]. The physical interpretation of Eq. (33) is that the internal state variable X of inductive response has an associated polarization process. This property is found in systems of different types [77,111,112]. Experimentally, this feature is associated with the observation of two positive arcs in the impedance response, as in Fig. 5(c).

Finally, the inductor element in Eq. (40) represents the coupling of ionic-electronic transport, as it contains the kinetic transport constants for both ions (D_X) and holes (μ_p). Because of the coexistence of different types of current, the impedance spectra acquire new shapes, as shown in Figs. 5(d)–5(f), with different possibilities of hysteresis patterns [104] and a time transient response to a voltage perturbation [111].

The analysis of Ref. [104] reveals that the chemical inductor structure in Eq. (34) is due to ionic diffusion. Many models of solar cells already use advanced explicit modeling by drift-diffusion of electronic and ionic currents and surface polarization to explain hysteresis in halide perovskite solar cells [17,52,92,113,114]. However, in the two-contact structure of a photovoltaic device, the ionic and electronic currents respond simultaneously to the applied voltage, and it is difficult to disentangle their coupling. In contrast, an orthogonal transistor structure separates both components and shows their coupling in the inductor response: The current between the source electrode and the drain electrode is delayed by the slower action of the ion insertion process stimulated by the gate electrode.

It is interesting to recognize that the complex modeling approaches [17,92,113] must contain the simplified structure of Eqs. (23) and (24), insofar as they give capacitive and inductive hysteresis. However, this underlying structure of the models may not be evident in many cases, due to the large number of simulation equations and parameters required in the mechanistic modeling, such as with the Ion-Monger package [115]. This question is further addressed in Sec. IX.

VII. TRANSITION FROM CAPACITIVE TO INDUCTIVE HYSTERESIS

In some systems we can have a hysteresis effect of a single kind, such as the capacitor corresponding to Fig. 1(C). However, in many more complex devices, such as memristors or solar cells, there will be a mixture of the two kinds, as is evident from the basic equivalent circuits in Figs. 2(a), 2(e), and 5(g).

In the set process of a memristor, the resistance decreases, and in the reset process, the current must return to the high-resistance value. Consequently, there is a crossing of the current, and a change of hysteresis from capacitive to inductive [40,116]. This process is very well illustrated in Fig. 4(a), where the change occurs near $V = 0$, and the transition of the impedance from capacitive, at negative voltage, to inductive, at positive voltage, is neat. More generally, the hysteresis properties can change along the current-voltage curve, and the hysteresis can switch between capacitive and inductive sectors, with associated crossings of the curve in different voltage domains [14,15,18,81]. In Fig. 1(B) the set process of the memristor is at a positive voltage, and the reset cycle is at negative voltages. In other reported memristors [117] the switch to high current occurs at negative polarity, with associated inverted hysteresis. It is also possible to exchange the side of the inductive process in an electrolytic system, as mentioned before [8].

To show clearly the transition from capacitive to inductive hysteresis, we analyze measurements of a fluorine-doped tin oxide (FTO)/poly(3,4-ethylenedioxythiophene) polystyrene sulfonate (PEDOT:PSS)/ $\text{CH}_3\text{NH}_3\text{PbBr}_3/\text{Au}$ memristor device as shown in Fig. 6(A). In Figs. 6(A)(a)–(A)(c), the highest voltage of the scan is successively increased. In the case of 0.25 V, the set process is not induced and the hysteresis loop is fully capacitive. Up to 0.75 V the crossing is observed, with the change of hysteresis causing the crossing of the curve. Up to 1.25 V the large inverted hysteresis loop characteristic of memristors is observed.

The impedance spectroscopy measurements in Figs. 6(A)(g)–(A)(i) capture these features well. At 0 V the impedance consists of two separate capacitive arcs. The low-frequency arc is related to the ionic distribution at the interface [118,119], and the structure of the equivalent circuit is that in Fig. 2(e), which produces the feature of Fig. 5(c) [77]. At 0.3 V the transition occurs: the low-frequency arc vanishes and starts to cross to the fourth quadrant. At 0.6 V the inductive arc is fully formed. These features have been described for halide perovskite memristors [11,96].

The possible causes and effects of inverted hysteresis have been amply discussed in halide perovskite solar cells [12,17–21]. Here we remark that the transition from capacitive to inductive hysteresis is reported for a FTO/ $\text{CH}_3\text{NH}_3\text{PbBr}_3/2,2',7,7'$ -Tetrakis[N,N-di(4-methoxyphenyl)amino]-9,9'-spirobifluorene (spiro-OMeTAD) solar cell in the dark [14], as shown in Fig. 6(B)(a). The evolution of the impedance spectra in Figs. 6(B)(c)–(B)(e) shows the same trend as that in Figs. 6(A)(g)–(A)(i): the low-frequency capacitive arc disappears and becomes an inductor.

In addition, a remarkable result was found that establishes a link between the low-frequency arc at low voltage, with capacitive time constant τ_C , and the high-voltage

inductor, with inductive time constant τ_L [14]. As noted in Fig. 6(B)(b), there is a continuity of the time constants across the transition, in which $\tau_C = \tau_L$, even though each time constant is measured in a separate voltage domain. This result was explained in a later publication [77] in terms of the models that contain a state variable X that forms both the inductive response and a capacitive polarization with a current of the type dX/dt , as in the example of Eqs. (33) and (34). It was shown that in such a structure the additional line $R_A C_A$ appears in Fig. 2(e), which creates the low-frequency capacitive arc. Furthermore, it was established that the equivalent circuit elements satisfy the identity

$$\tau_C = R_A C_A = \tau_L = \frac{L_a}{R_a} \quad (41)$$

as obtained experimentally; see Fig. 6(B)(b).

The result [77] elucidates why a low-frequency capacitor and inductor are correlated: They correspond to the same physical variable. This behavior of the transition from capacitive to inductive hysteresis, accompanied by the transformation of the type of the low-frequency arc, has also been obtained in very different devices as nanofluidic porous membranes [112]. It appears to be a model of general significance.

We mention additional possibilities of interplay between capacitive and inductive hysteresis along the current-voltage curve. Figure 7(a) shows hysteresis behavior for a halide perovskite FTO/PEDOT:PSS/ $\text{CH}_3\text{NH}_3\text{PbI}_3/\text{Au}$ memristor under illumination [81]. At positive voltage in Fig. 7(a) the device displays the typical large inductive loop that corresponds to the resistive switching of the memristor. Around the origin there is a strong capacitive process, and at negative potentials an additional inductive domain is found. These features are well correlated with the type of impedance spectrum that is obtained in each voltage domain; see Figs. 7(b) and 7(c). In the region of low voltages, the spectra show a double-arc feature, which can be well described by the additional slow variable in the model, that undergoes polarization, as mentioned above [77]. At very positive and very negative voltages we observe clearly the inductive features in the fourth quadrant that generate the respective inverted hysteresis domains.

In summary, the analysis of different systems shows that impedance spectroscopy characterization is useful to predict and quantify the hysteresis trends that are obtained in current-voltage curves.

VIII. STEPWISE RESPONSE IN THE TIME-DOMAIN INTERPRETATION OF HYSTERESIS

An additional method to probe the hysteresis properties is to apply consecutive small steps of the voltage and

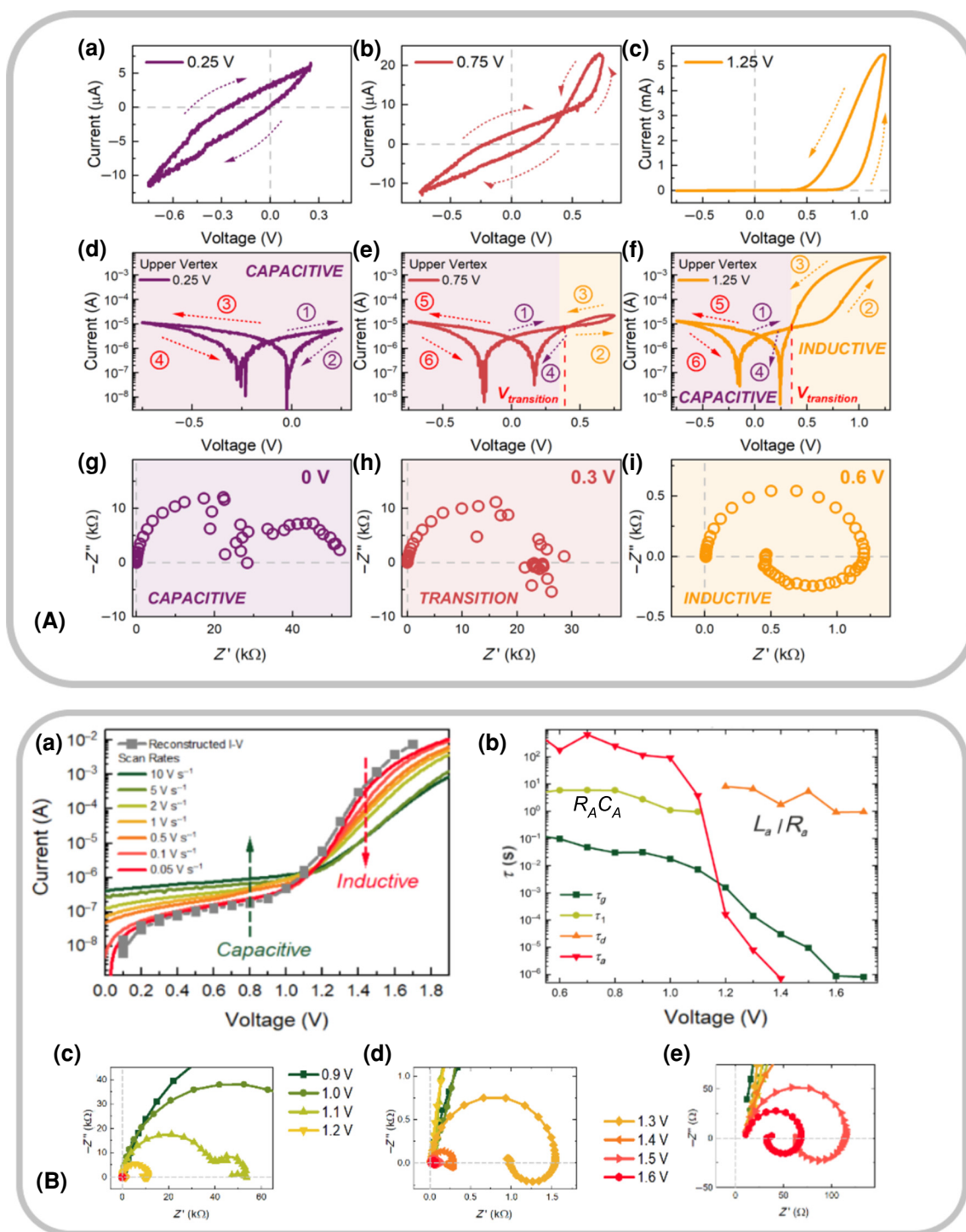


FIG. 6. (A) Characteristic I - V response on a linear scale of the FTO/PEDOT:PSS/CH₃NH₃PbBr₃/Au memristor device with differing upper vertex voltages of (a) 0.25 V, (b) 0.75 V, and (c), 1.25 V, with the arrows indicating the scan direction. Corresponding I - V response on a semilogarithmic scale for upper vertex voltages of (d) 0.25 V, (e) 0.75, and (f) 1.25 V, with the arrows and numbers indicating the scan direction and sequence, respectively. Voltage-dependent impedance spectral evolution measured at (g) 0 V, (h) 0.3 V, and (i) 0.6 V exhibiting a transition from a low-frequency capacitive response at low applied voltages to a low-frequency inductive response at high applied voltages. Figure courtesy of Cedric Gonzales. (B) Results of the measurement of a perovskite solar cell with structure FTO/CH₃NH₃PbBr₃/spiro-OMeTAD in the dark. (a) Evolution of hysteresis at different scan rates in the forward direction on a logarithmic vertical scale in the dark. (b) Time constants resulting from the impedance parameters as a function of cell voltage. Two time constants are indicated in the nomenclature of the present paper: $R_A C_A$ and L_a / R_a . Reproduced with permission from C. Gonzales, A. Guerrero, J. Bisquert, J. Phys. Chem. C 126, 13560–13578 (2022). Licensed under a Creative Commons Attribution (CC BY 4.0) license.

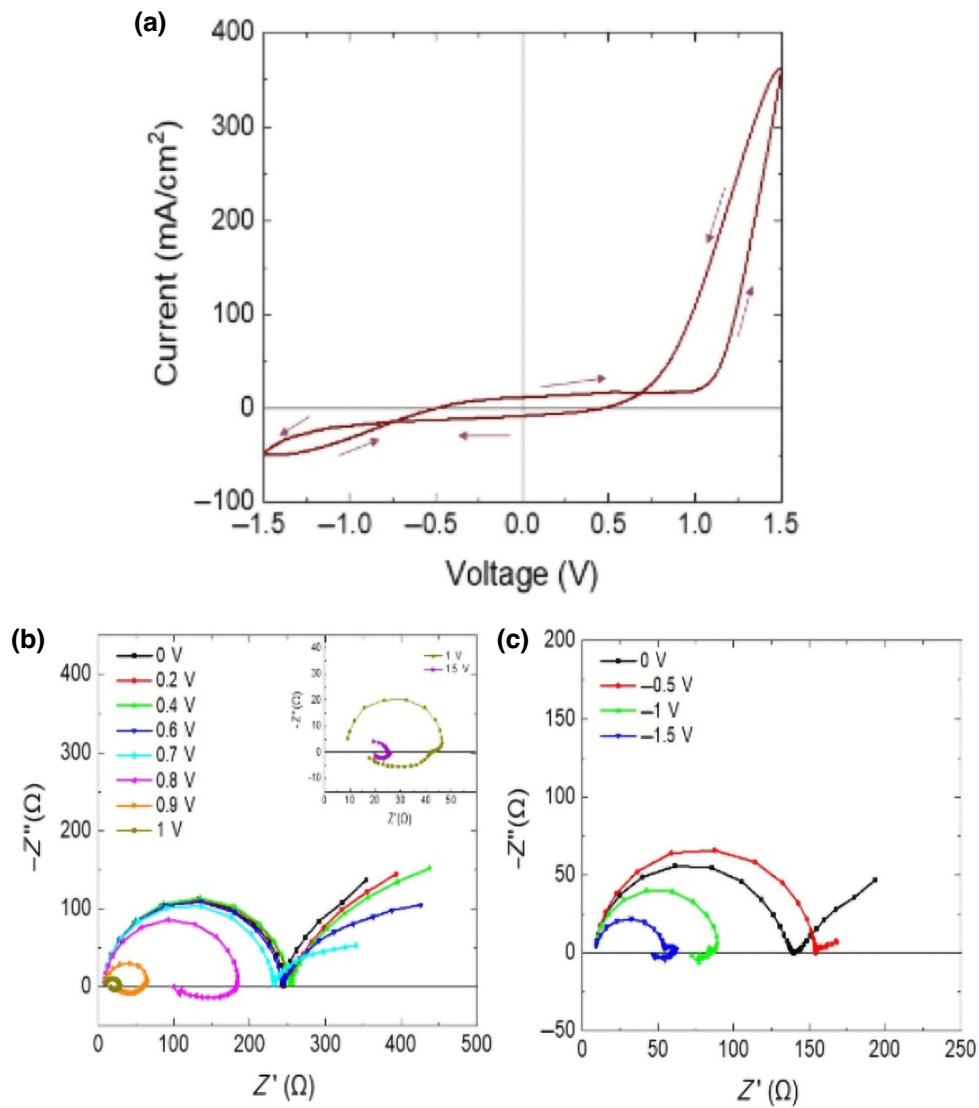


FIG. 7. (a) Current density–voltage characteristic measured at 50 mW/cm² blue light illumination for a FTO/PEDOT:PSS/CH₃NH₃PbI₃/Au memristor. Arrows indicate the sweep direction. (b),(c) Corresponding complex plane plot representation of the impedance spectra at various dc voltages, measured from 1 MHz to 0.1 Hz. The inset corresponds to higher dc voltages applied. Reproduced with permission from L. Munoz-Diaz, A. J. Rosa, A. Bou, R. S. Sanchez, B. Romero, R. A. John, M. V. Kovalenko, A. Guerrero, J. Bisquert, *Front. Energy Res.* 10, 914115 (2022). Licensed under a Creative Commons Attribution (CC BY 4.0) license.

monitor the correspondent current response. This approach is shown in Figs. 1(A)(b) and 1(A)(c) for the measurement of the halide perovskite solar cell [2,25,120]. This stepwise procedure is inherent in the “continuous” voltage scan assumed in the linear sweep technique corresponding to Eq. (1), as the instrument produces discrete voltage steps. This is illustrated in Fig. 8(A), showing the stepwise property of the voltage ramp [25]. The global observed hysteresis of the current-voltage curve in Fig. 8(A)(c) may then be understood in terms of elementary relaxation phenomena occurring in the individual steps, as observed in Fig. 8(A)(b). This method is the

basis for determination of the stabilization of the current in high-throughput evaluation of performance by tracking the maximum power point [34].

While stepwise measurements have been reported in many cases as shown in Figs. 1(A) and 8(A), a quantitative explanation of the resulting hysteresis has not been provided, as far as we know. In the literature, the transient response to each voltage step is analyzed with use of exponential decays [34], which will not work in the case of inductive hysteresis. Recently, we discussed the transient response of models of the type of Eqs. (23) and (24) to a voltage step [121]. To elucidate the origin of inductive and

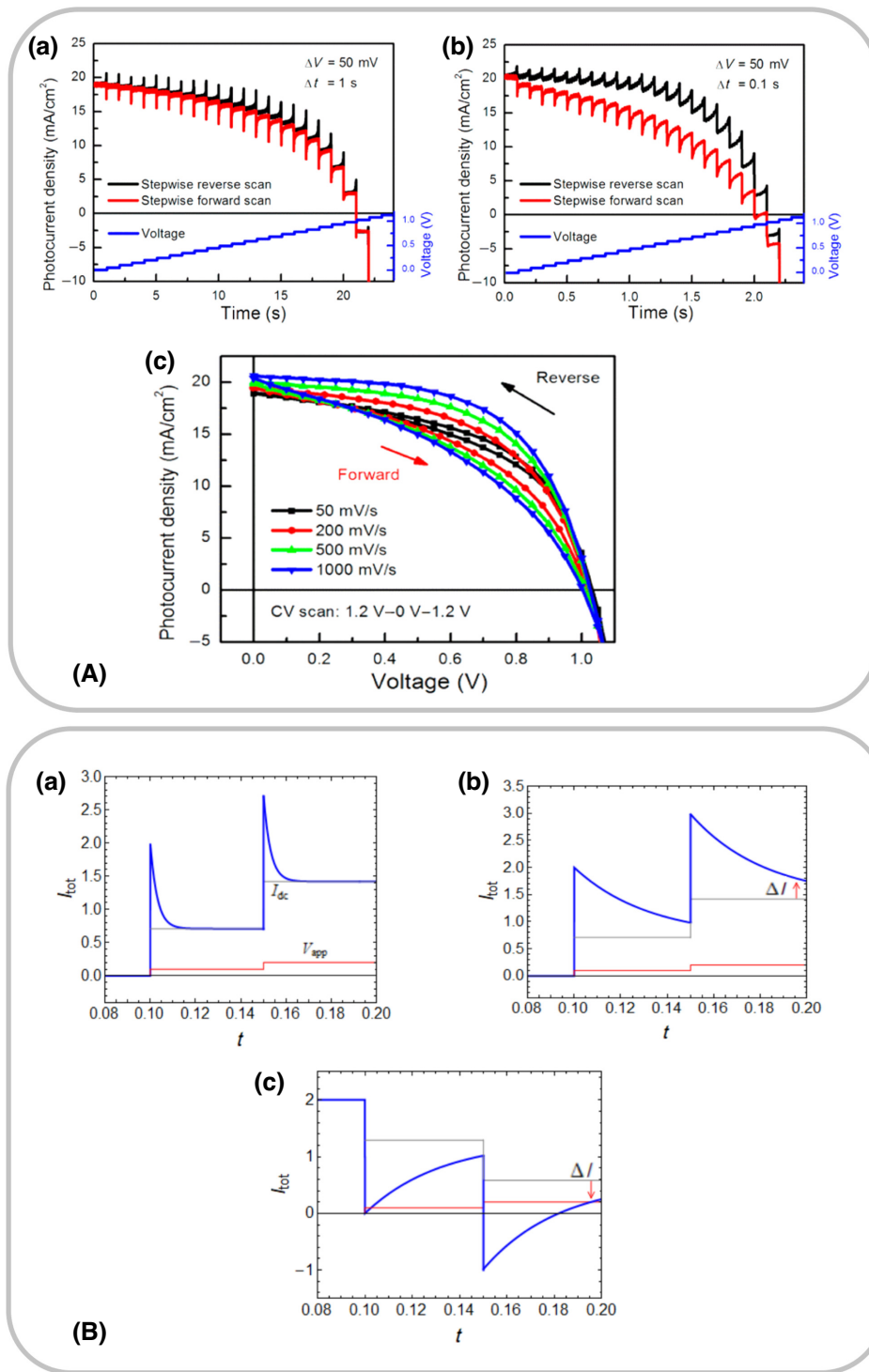


FIG. 8. (A) Time-dependent photocurrent response of a planar perovskite solar cell on compact TiO_2 with 500-nm $\text{CH}_3\text{NH}_3\text{PbI}_3$ film as the light-absorber layer and 150-nm spiro-OMeTAD as the hole transport layer under reverse and forward stepwise scans with (a) 1-s step time and (b) 0.1-s step time. (c) Current-voltage response with different scan rates. CV, cyclic voltammetry. Reproduced with permission from B. Chen, M. Yang, X. Zheng, C. Wu, W. Li, Y. Yan, J. Bisquert, G. Garcia-Belmonte, K. Zhu, S. Priya, *J. Phys. Chem. Lett.* 6, 4693–4700 (2015). Copyright 2015, American Chemical Society. (B) Current response of the linear model to two consecutive voltage steps, from time t_0 , of duration Δt , the first with amplitude $\Delta V = 0.1$ and the second with amplitude $\Delta V = 0.2$. The common parameters are $R_b = 1$, $R_a = 0.1$, $R_s = 0.05$, $t_0 = 0.1$, $\Delta t = 0.05$, and $\tau_k = 0.0005$. The different cases are (a) $C_m = 0.1$, (b) $C_m = 1$, and (c) $C_m = 1$, and added photocurrent $I_{\text{photo}} = 2$. The red lines indicate the applied voltage steps and the gray lines indicate the steady-state current at the given voltage. The orange arrows indicate the excess current at the end of the cycle with respect to the steady-state value. The curves in (B) are given in arbitrary units to illustrate the general shapes caused by the indicated parameters.

capacitive hysteresis in terms of elementary relaxations, we now apply a similar method to the linear model of Eqs. (9) and (10), represented as the equivalent circuit in Fig. 2(a).

When a voltage step is imposed on the conducting system, it is important to consider the presence of the series resistance, as indicated in Fig. 2(a). Then the applied voltage V_{app} is divided between the active zone voltage, u , and the series resistance, as follows:

$$V_{app} = R_s I_{tot} + u. \quad (42)$$

We apply two consecutive voltage steps $\Delta V, 2\Delta V$ of duration Δt and measure the current. The results of the calculation are shown in Fig. 8(B) for a system in which the inductive process is very fast and can be ignored, so

that the time response is dominated by the capacitance and resistors. In each diagram the gray line is the stationary current that can be expected at the given applied voltage, i.e.,

$$I_{dc} = \frac{V_{app}}{R_{tot}}, \quad (43)$$

where

$$R_{tot} = R_s + \left(\frac{1}{R_b} + \frac{1}{R_a} \right)^{-1}. \quad (44)$$

We observe that when a voltage step is applied at t_0 in Fig. 8(B)(a), there is a capacitive peak. This is because in the initial instant the capacitor is discharged and all the

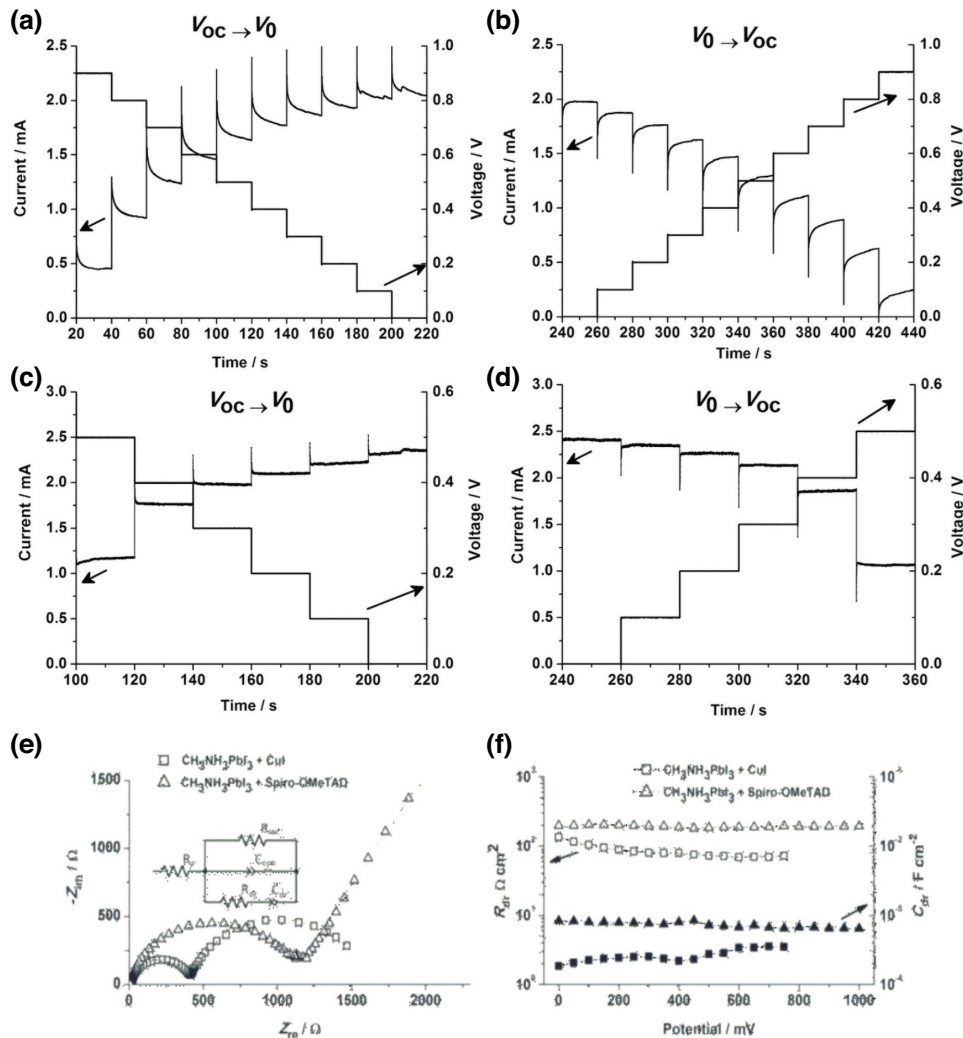


FIG. 9. Steady-state current measurements using forward and reverse stepwise voltage sweeps for two metal halide perovskite solar cells differing in the contact: (a),(b) spiro-OMeTAD and (c),(d) CuI-based. (e) Complex plane impedance plots for the two devices, and fit to the equivalent circuit model. (f) Variation in low-frequency resistance and capacitance in both devices. Impedance measurements were performed under constant illumination. OC, open circuit. Reproduced with permission from G. A. Sepalage, S. Meyer, A. Pascoe, A. D. Scully, F. Huang, U. Bach, Y.-B. Cheng, L. Spiccia, Adv. Funct. Mater. 25, 5650–5661 (2015). Copyright 2015, Wiley.

voltage goes to the series resistance [121], so the initial peak height is $\Delta V/R_s$. Thereafter the capacitor charges with a characteristic time $\tau_C = R_s C_m$, until the equilibrium current I_{dc} is reached. The next increase ΔV raises the current again. In Fig. 8(B)(b) the capacitance is 10 times larger, so the charging time is 10 times longer. The charging cannot be completed in each step, and a difference ΔI is accumulated at the end point. This is the *positive* capacitive hysteresis current.

We remarked regarding Eq. (31) that the representation of the photocurrent in a solar cell is inverted with respect to the dark current. For Fig. 8(B)(c), we apply Eq. (31) and flip the capacitive peaks, so that ΔI becomes negative. The resulting pattern explains well the current response to voltage steps in a forward scan in Figs. 1(A)(b) and 8(A)(b). We can deduce from the model that in a faster scan, the steps will be shorter in time, and the accumulated deficit of current will be larger. This is the property of capacitive hysteresis that is observed in Fig. 8(A)(c).

For Fig. 9 the step procedure is applied to two perovskite devices that differ in the hole extraction contact [120]. In the first cell [Figs. 9(a) and 9(b)] the relaxation is not completed in each step and the sample shows significant hysteresis. In the second case [Figs. 9(c) and 9(d)] the charging time τ_C of the capacitor is much shorter, so the hysteresis is reduced. This was achieved by decrease of both the low-frequency resistance and the capacitance, as shown in Fig. 9(f).

We now turn our attention to the influence of the inductor in the step response of the current, shown in Fig. 10. The transient begins with a capacitive peak, as in the former case, but now additional parallel resistance R_a is activated when the inductor responds in time of order τ_L [121]. Hence, the current increases with time until the equilibrium current is reached; see Fig. 10(a). In Fig. 10(b)

the inductor time is longer, and the final current cannot be achieved. This produces a total negative deficit, which explains the property of negative hysteresis in terms of the elementary step behavior. A full classification of the time-domain response when several inductive and capacitive elements act in concert was presented in Ref. [111].

In summary, capacitive and inductive processes provide opposite types of time transient response. This is closely related to the different frequency-domain response of both elements indicated in Figs. 3(c) and 3(e). In a capacitive process the impedance decreases at increasing frequency. Correspondingly, the current of capacitive charging decreases with time. However, the impedance of the inductor decreases at lower frequency. Consequently, the current of the inductive process *increases* with time, as shown in Fig. 10. The inductive property is an essential component of the phenomenon of synapse potentiation that is necessary for neuromorphic computation elements [8,112,121–123].

IX. THE FREQUENCY DEPENDENCE OF HYSTERESIS

In this section we comment on the manifestation of hysteresis as a function of the frequency Ω_s of measurement of current-voltage curves [114]. This is shown in Fig. 11(A) for the porous nanochannels of Fig. 4 [8]. The voltage is scanned by a sinusoidal wave. At low frequencies the full stationary current is observed, but at higher frequencies at positive voltage the inductive hysteresis becomes significant and the current remains lower due to removal of the slow-response component.

We consider an important result shown in Fig. 11(B) [72], which illustrates the correspondence of the hysteresis effect and the frequency of measurement, according to the

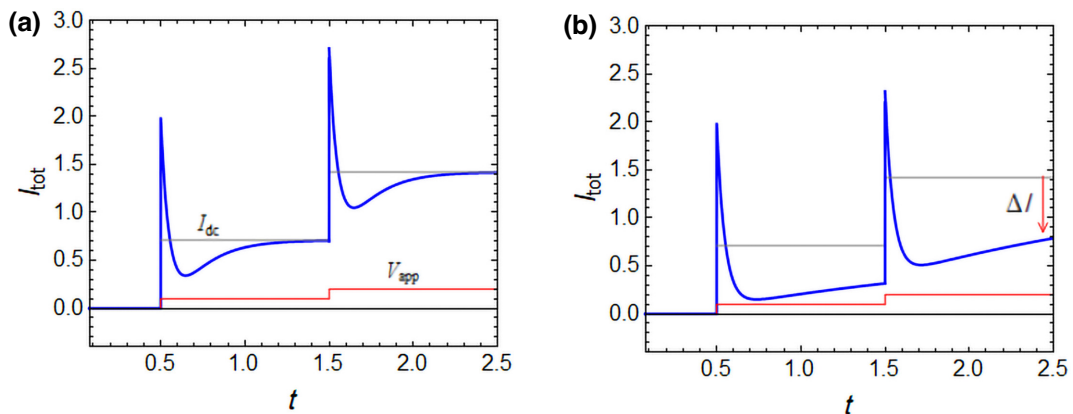


FIG. 10. Current response of the linear model to two consecutive voltage steps, from time t_0 , of duration Δt , the first with amplitude $\Delta V = 0.1$ and the second with amplitude $\Delta V = 0.2$. The common parameters are $R_b = 1$, $R_a = 0.1$, $R_s = 0.05$, $t_0 = 0.5$, $\Delta t = 1$, and $C_m = 1$. The different cases are (a) $\tau_k = 0.3$ and (b) $\tau_k = 3$. The red lines indicate the applied voltage steps and the gray lines indicate the steady-state current at the given voltage. The orange arrows indicate the excess current at the end of the cycle with respect to the steady-state value. The curves are given in arbitrary units to illustrate the general shapes caused by the indicated parameters.

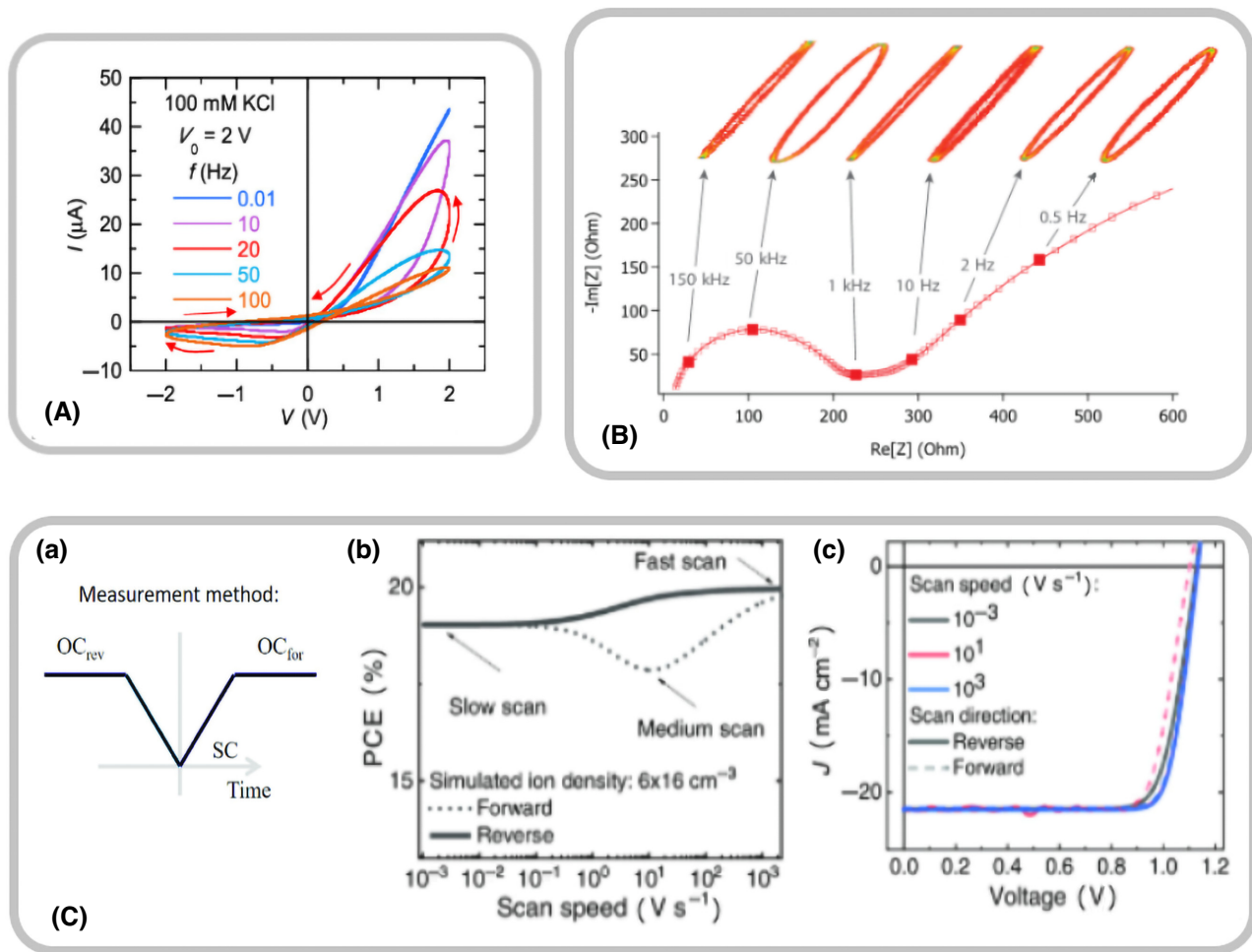


FIG. 11. (A) (a) I - V curves for a multipore membrane in 100 mM KCl solution at neutral pH , parametrically in the electrical potential scan rate, characterized by the signal frequency $f = \Omega_s/2\pi$, obtained with a voltage amplitude of 2 V. The arrows indicate the signal time evolution. Reproduced with permission from P. Ramirez, V. Gomez, J. Cervera, S. Mafe, J. Bisquert, *J. Phys. Chem. Lett.* 14, 10930–10934 (2023). Copyright 2023, American Chemical Society. (B) Complex plane plot of the impedance of a $CH_3NH_3PbI_3$ -based mesoscopic solar cell, measured at 950 mV under equivalent 1000 W m^{-2} solar irradiation. The Lissajous curves (current versus voltage) corresponding to a sinusoidal perturbation ($V_{rms} = 22 \text{ mV}$) under the same measuring conditions (light and dc bias) are shown at the top for the indicated frequencies. Reproduced with permission from N. Pellet, F. Giordano, M. I. Dar, G. Gregori, S. M. Zakeeruddin, J. Maier, M. Grätzel, *Prog. Photovolt. Res. Appl.* 25, 942–950 (2017). Copyright 2017, Wiley. (C) Simulation of halide perovskite solar cell hysteresis at different scan velocities. (a) Measurement procedure to record the current-voltage curves and band diagrams starting at open-circuit voltage (OC) and progressing to short-circuit current (SC) and back. (b) Simulated fast-hysteresis power conversion efficiency plot in forward and reverse scans and the characteristic efficiencies at slow, medium, and fast scan speeds. (c) Corresponding simulated current-voltage curves. Reproduced with permission from V. M. Le Corre, J. Diekmann, F. Peña-Camargo, J. Thiesbrummel, N. Tokmoldin, E. Gutierrez-Partida, K. P. Peters, L. Perdigón-Toro, M. H. Futscher, F. Lang, J. Warby, H. J. Snaith, D. Neher, M. Stollerfoht, *Solar RRL* 6, 2100772 (2022). Copyright 2022, Wiley.

type of impedance response that prevails at the frequency chosen. By changing the cycling of the current-voltage curve (with a small amplitude of 22 mV), we change the point of measurement in the complex plane plot of the impedance. It is observed that when the imaginary part of the impedance becomes large, corresponding to a capacitive response at this frequency, the hysteresis increases, as shown in the Lissajous curves. In Fig. 11(B) the two components introducing time lag in the respective arcs

(one at low and another one at high frequency) are capacitive, corresponding to the model of Figs. 2(e) and 5(c). The low-frequency inductor response is not presented in Fig. 11(B), although it could exist, but the impedance is not reported up to very low frequency. If we measure up to such a low frequency, and find the inductor component, we can infer that the inductive feature of the hysteresis could appear, causing the Lissajous figure to spin in the opposite direction, as shown in Fig. 3.

Figure 11(C) shows a study of the hysteresis traits of drift-diffusion simulated halide perovskite operation, which corresponds well to the experimental observations in the same work [113]. The solar cell is stabilized at open-circuit voltage and then measured in reverse and forward cycles, as shown in Fig. 11(C)(a). The PCE is larger in the reverse scan, so this model contains only capacitive hysteresis, as discussed in Sec. V, and the impedance picture must be the same as in Fig. 11(B). The trend of hysteresis as a function of frequency shown Fig. 11(C)(b) is the same as that in Fig. 11(B): the system surmounts a capacitive arc centered at a scan rate of 10 V s^{-1} . At a high frequency of the scan, the system becomes a pure resistance, and the total PCE increases slightly. This is because the low-frequency arc in Fig. 11(B) has been removed, and it means that the low-frequency arc is deleterious for the performance, because it is a recombination loss at the contacts, caused by the ionic distribution, that is avoided in the fast measurement. In the study in Ref. [114], the efficiency and hysteresis increase at increasing frequency as in Fig. 11(C), but then start to decrease at the highest frequencies. This means that the scan is affecting the high-frequency arc that holds the PCE of the solar cell. However, the previous considerations should be regarded as preliminary intuitive explanations. In the voltage scan the system changes over a wide voltage range that covers a large variation of the impedance parameters [63,124], and a detailed quantitative transformation between the time domain and the frequency domain becomes necessary [11].

We remark that one can obtain a transition of the kind of hysteresis (capacitive to inductive or vice versa) in two different ways: by changing the voltage modifying the dominant low-frequency component, as shown in Fig. 6, or by operating at a fixed voltage, by changing the frequency of the measurement of the current-voltage curve, as in Fig. 11.

X. CONCLUSION

Our comprehensive exploration has unveiled the intricate nature of hysteresis across a spectrum of electronic, ionic, and mixed ionic-electronic devices. Through a multidimensional approach, we have delineated two fundamental hysteresis archetypes—capacitive and inductive—rooted in distinctive transient responses. These archetypes, revealed through diverse analytical methods, provide a unifying framework to decipher hysteresis in systems as disparate as solar cells, capacitors, transistors, and ion channels. Furthermore, the use of complementary methods facilitates the prediction and classification of more concrete physical and molecular models that account for the complicated evolution of the current with time in highly heterogeneous and nonlinear systems.

Our analysis provides a criterion for making these advanced physical models, such as those elaborated by

drift-diffusion equations and polarization assumptions. From the knowledge of basic structural conditions for equations that produce capacitive and inductive hysteresis and their combinations, we have a yardstick to measure advanced physical models that contain specific physical effects. We can first determine the evolution of hysteresis in an experimental system using the frequency analysis and general descriptive models, and can then develop concrete specific explanations that satisfy the overall behavior. We emphasize that the fact that a model providing some type of description of hysteresis is not enough to validate such a model. Many equivalent models can be made, provided that they satisfy the basic structural conditions that give the right evolution of the equivalent circuit. A more stringent test of models and theories is needed, at least considering a variety of experimental response methods.

By elucidating the underlying mechanisms driving hysteresis, we increase our understanding of its pervasive presence in both natural and engineered contexts, contributing to the broader understanding of dynamic responses in complex systems.

ACKNOWLEDGMENTS

This work was funded by the European Research Council via Advanced Grant No. 101097688 (PeroSpiker). I am grateful for discussions with Agustín Bou, Antonio Guerrero, Cedric Gonzales, Enrique Hernández-Balaguera, and Patricio Ramirez.

-
- [1] H. J. Snaith, A. Abate, J. M. Ball, G. E. Eperon, T. Leijtens, N. K. Noel, S. D. Stranks, J. T.-W. Wang, K. Wojciechowski, and W. Zhang, Anomalous hysteresis in perovskite solar cells, *J. Phys. Chem. Lett.* **5**, 1511 (2014).
 - [2] H.-S. Kim and N.-G. Park, Parameters affecting $I-V$ hysteresis of $\text{CH}_3\text{NH}_3\text{PbI}_3$ perovskite solar cells: Effects of perovskite crystal size and mesoporous TiO_2 layer, *J. Phys. Chem. Lett.* **5**, 2927 (2014).
 - [3] S. van Reenen, M. Kemerink, and H. J. Snaith, Modeling anomalous hysteresis in perovskite solar cells, *J. Phys. Chem. Lett.* **6**, 3808 (2015).
 - [4] R. B. Nuernberg, N. M. P. Machado, D. Jouglard, L. del Campo, M. Malki, and M. Neyret, The origin of hysteresis in the electrical behavior of RuO_2 -glass composite melts, *J. Non-Cryst. Solids* **557**, 120596 (2021).
 - [5] W. Brown, M. Kvetny, R. Yang, and G. Wang, Selective ion enrichment and charge storage through transport hysteresis in conical nanopipettes, *J. Phys. Chem. C* **126**, 10872 (2022).
 - [6] K. Intonti, E. Faella, L. Viscardi, A. Kumar, O. Durante, F. Giubileo, M. Passacantando, H. T. Lam, K. Anastasiou, M. F. Craciun, S. Russo, and A. Di Bartolomeo, Hysteresis and photoconductivity of few-layer ReSe_2 field effect transistors enhanced by air pressure, *Adv. Electron. Mater.* **9**, 2300066 (2023).

- [7] R. Shameem, L. M. Bongartz, A. Weissbach, H. Kleemann, and K. Leo, Hysteresis in organic electrochemical transistors: Relation to the electrochemical properties of the semiconductor, *Appl. Sci.* **13**, 5754 (2023).
- [8] P. Ramirez, V. Gomez, J. Cervera, S. Mafe, and J. Bisquert, Synaptical tunability of multipore nanofluidic memristors, *J. Phys. Chem. Lett.* **14**, 10930 (2023).
- [9] A. Migliore and A. Nitzan, Irreversibility and hysteresis in redox molecular conduction junctions, *J. Am. Chem. Soc.* **135**, 9420 (2013).
- [10] G. Garcia-Belmonte and J. Bisquert, Distinction between capacitive and noncapacitive hysteretic currents in operation and degradation of perovskite solar cells, *ACS Energy Lett.* **1**, 683 (2016).
- [11] J. Bisquert, A. Guerrero, and C. Gonzales, Theory of hysteresis in halide perovskites by integration of the equivalent circuit, *ACS Phys. Chem. Au* **1**, 25 (2021).
- [12] W. Tress, J. P. Correa Baena, M. Saliba, A. Abate, and M. Graetzel, Inverted current–voltage hysteresis in mixed perovskite solar cells: Polarization, energy barriers, and defect recombination, *Adv. Energy Mater.* **6**, 1600396 (2016).
- [13] V. Lopez-Richard, R. S. Wengenroth Silva, O. Lipan, and F. Hartmann, Tuning the conductance topology in solids, *J. Appl. Phys.* **133**, 134901 (2023).
- [14] C. Gonzales, A. Guerrero, and J. Bisquert, Transition from capacitive to inductive hysteresis: A neuron-style model to correlate I – V curves to impedances of metal halide perovskites, *J. Phys. Chem. C* **126**, 13560 (2022).
- [15] Nicolae Filipoiu, A. T. P. Dragos-Victor Anghel, Roxana Patru, Rachel Elizabeth Brophy, Movaffaq Kateb, Cristina Besleaga, Andrei Gabriel Tomulescu, Ioana Pintilie, Andrei Manolescu, and George Alexandru Nemnes, Capacitive and inductive effects in perovskite solar cells: The different roles of ionic current and ionic charge accumulation, *Phys. Rev. Appl.* **18**, 064087 (2022).
- [16] A. O. Alvarez, R. Arcas, C. A. Aranda, L. Bethencourt, E. Mas-Marzá, M. Saliba, and F. Fabregat-Santiago, Negative capacitance and inverted hysteresis: Matching features in perovskite solar cells, *J. Phys. Chem. Lett.* **11**, 8417 (2020).
- [17] W. Clarke, M. V. Cowley, M. J. Wolf, P. Cameron, A. Walker, and G. Richardson, Inverted hysteresis as a diagnostic tool for perovskite solar cells: Insights from the drift-diffusion model, *J. Appl. Phys.* **133**, 095001 (2023).
- [18] G. A. Nemnes, C. Besleaga, V. Stancu, D. E. Dogaru, L. N. Leonat, L. Pintilie, K. Torfason, M. Ilkov, A. Manolescu, and I. Pintilie, Normal and inverted hysteresis in perovskite solar cells, *J. Phys. Chem. C* **121**, 11207 (2017).
- [19] R. A. Belisle, W. H. Nguyen, A. R. Bowring, P. Calado, X. Li, S. J. C. Irvine, M. D. McGehee, P. R. F. Barnes, and B. C. O'Regan, Interpretation of inverted photocurrent transients in organic lead halide perovskite solar cells: Proof of the field screening by mobile ions and determination of the space charge layer widths, *Energy Environ. Sci.* **10**, 192 (2017).
- [20] H. Shen, D. A. Jacobs, Y. Wu, T. Duong, J. Peng, X. Wen, X. Fu, S. K. Karuturi, T. P. White, K. Weber, and K. R. Catchpole, Inverted hysteresis in $\text{CH}_3\text{NH}_3\text{PbI}_3$ solar cells: Role of stoichiometry and band alignment, *J. Phys. Chem. Lett.* **8**, 2672 (2017).
- [21] D. Moia, I. Gelmetti, P. Calado, W. Fisher, M. Stringer, O. Game, Y. Hu, P. Docampo, D. Lidzey, E. Palomares, J. Nelson, and P. R. F. Barnes, Ionic-to-electronic current amplification in hybrid perovskite solar cells: Ionically gated transistor-interface circuit model explains hysteresis and impedance of mixed conducting devices, *Energy Environ. Sci.* **12**, 1296 (2019).
- [22] H.-S. Kim, I.-H. Jang, N. Ahn, M. Choi, A. Guerrero, J. Bisquert, and N.-G. Park, Control of I – V hysteresis in $\text{CH}_3\text{NH}_3\text{PbI}_3$ perovskite solar cell, *J. Phys. Chem. Lett.* **6**, 4633 (2015).
- [23] E. L. Unger, E. T. Hoke, C. D. Bailie, W. H. Nguyen, A. R. Bowring, T. Heumüller, M. G. Christoforo, and M. D. McGehee, Hysteresis and transient behavior in current–voltage measurements of hybrid-perovskite absorber solar cells, *Energy Environ. Sci.* **7**, 3690 (2014).
- [24] O. Almora, C. Aranda, I. Zarazua, A. Guerrero, and G. Garcia-Belmonte, Noncapacitive hysteresis in perovskite solar cells at room temperature, *ACS Energy Lett.* **1**, 209 (2016).
- [25] B. Chen, M. Yang, X. Zheng, C. Wu, W. Li, Y. Yan, J. Bisquert, G. Garcia-Belmonte, K. Zhu, and S. Priya, Impact of capacitive effect and ion migration on the hysteretic behavior of perovskite solar cells, *J. Phys. Chem. Lett.* **6**, 4693 (2015).
- [26] Y. G. Rong, Y. Hu, S. Ravishankar, H. W. Liu, X. M. Hou, Y. S. Sheng, A. Y. Mei, Q. F. Wang, D. Y. Li, M. Xu, J. Bisquert, and H. W. Han, Tunable hysteresis effect for perovskite solar cells, *Energy Environ. Sci.* **10**, 2383 (2017).
- [27] R. Marquardt, F. Zahari, J. Carstensen, G. Popkirov, O. Gronenberg, G. Kolhatkar, H. Kohlstedt, and M. Ziegler, Impedance spectroscopy on hafnium oxide-based memristive devices, *Adv. Electron. Mater.* **9**, 2201227 (2023).
- [28] O. Gharbi, M. T. T. Tran, B. Tribollet, M. Turmine, and V. Vivier, Revisiting cyclic voltammetry and electrochemical impedance spectroscopy analysis for capacitance measurements, *Electrochim. Acta* **343**, 136109 (2020).
- [29] S. Hagiwara, S. Miyazaki, and N. P. Rosenthal, Potassium current and the effect of cesium on this current during anomalous rectification of the egg cell membrane of a starfish, *J. Gen. Physiol.* **67**, 621 (1976).
- [30] E. Zimmermann, P. Ehrenreich, T. Pfadler, J. A. Dorman, J. Weickert, and L. Schmidt-Mende, Erroneous efficiency reports harm organic solar cell research, *Nat. Photonics* **8**, 669 (2014).
- [31] J. A. Christians, J. S. Manser, and P. V. Kamat, Best practices in perovskite solar cell efficiency measurements. Avoiding the error of making bad cells look good, *J. Phys. Chem. Lett.* **6**, 852 (2015).
- [32] Y. Wang, X. Liu, Z. Zhou, P. Ru, H. Chen, X. Yang, and L. Han, Reliable measurement of perovskite solar cells, *Adv. Mater.* **31**, 1803231 (2019).
- [33] F. Wu, R. Pathak, and Q. Qiao, Origin and alleviation of J-V hysteresis in perovskite solar cells: A short review, *Catal. Today* **374**, 86 (2021).
- [34] L. Rakocevic, F. Ernst, N. T. Yimga, S. Vashishtha, T. Aernouts, T. Heumueller, C. J. Brabec, R. Gehlhaar, and

- J. Poortmans, Reliable performance comparison of perovskite solar cells using optimized maximum power point tracking, *Sol. RRL* **3**, 1800287 (2019).
- [35] H. Köbler, S. Neubert, M. Jankovec, B. Glazar, M. Haase, C. Hilbert, M. Topič, B. Rech, and A. Abate, High-throughput aging system for parallel maximum power point tracking of perovskite solar cells, *Energy Technol.* **10**, 2200234 (2022).
- [36] L. O. Chua and K. Sung Mo, Memristive devices and systems, *Proc. IEEE* **64**, 209 (1976).
- [37] K. J. Kwak, D. E. Lee, S. J. Kim, and H. W. Jang, Halide perovskites for memristive data storage and artificial synapses, *J. Phys. Chem. Lett.* **12**, 8999 (2021).
- [38] K. Kang, W. Hu, and X. Tang, Halide perovskites for resistive switching memory, *J. Phys. Chem. Lett.* **12**, 11673 (2021).
- [39] Y. Fang, S. Zhai, L. Chu, and J. Zhong, Advances in halide perovskite memristor from lead-based to lead-free materials, *ACS Appl. Mater. Interfaces* **13**, 17141 (2021).
- [40] Y. V. Pershin and M. Di Ventra, Memory effects in complex materials and nanoscale systems, *Adv. Phys.* **60**, 145 (2011).
- [41] M. Rahimi Azghadi, Y.-C. Chen, J. K. Eshraghian, J. Chen, C.-Y. Lin, A. Amirsoleimani, A. Mehonic, A. J. Kenyon, B. Fowler, J. C. Lee, and Y.-F. Chang, Complementary metal-oxide semiconductor and memristive hardware for neuromorphic computing, *Adv. Intell. Syst.* **2**, 1900189 (2020).
- [42] K. Sun, J. Chen, and X. Yan, The future of memristors: Materials engineering and neural networks, *Adv. Funct. Mater.* **31**, 2006773 (2021).
- [43] Y. Wang, Q. Zhang, H. P. A. G. Astier, C. Nickle, S. Soni, F. A. Alami, A. Borriani, Z. Zhang, C. Honnigfort, B. Braunschweig, A. Leoncini, D.-C. Qi, Y. Han, E. del Barco, D. Thompson, and C. A. Nijhuis, Dynamic molecular switches with hysteretic negative differential conductance emulating synaptic behaviour, *Nat. Mater.* **21**, 1403 (2022).
- [44] A. Kumar, L. Viscardi, E. Faella, F. Giubileo, K. Intonti, A. Pelella, S. Sleziona, O. Kharsah, M. Schleberger, and A. Di Bartolomeo, Temperature dependent black phosphorus transistor and memory, *Nano Express* **4**, 014001 (2023).
- [45] H. Ling, D. A. Koutsouras, S. Kazemzadeh, Y. van de Burgt, F. Yan, and P. Gkoupidenis, Electrolyte-gated transistors for synaptic electronics, neuromorphic computing, and adaptable biointerfacing, *Appl. Phys. Rev.* **7**, 011307 (2020).
- [46] X. Liang, Y. Luo, Y. Pei, M. Wang, and C. Liu, Multimode transistors and neural networks based on ion-dynamic capacitance, *Nat. Electron.* **5**, 859 (2022).
- [47] J. Rivnay, S. Inal, A. Salleo, R. M. Owens, M. Berggren, and G. G. Malliaras, Organic electrochemical transistors, *Nat. Rev. Mater.* **3**, 17086 (2018).
- [48] R. B. Rashid, X. Ji, and J. Rivnay, Organic electrochemical transistors in bioelectronic circuits, *Biosens. Bioelectron.* **190**, 113461 (2021).
- [49] K. Sakhatskyi, R. A. John, A. Guerrero, S. Tsarev, S. Sabisch, T. Das, G. J. Matt, S. Yakunin, I. Cherniukh, M. Kotyrba, Y. Berezovska, M. I. Bodnarchuk, S. Chakraborty, J. Bisquert, and M. V. Kovalenko, Assessing the drawbacks and benefits of ion migration in lead halide perovskites, *ACS Energy Lett.* **7**, 3401 (2022).
- [50] A. Senocrate and J. Maier, Solid-state ionics of hybrid halide perovskites, *J. Am. Chem. Soc.* **141**, 8382 (2019).
- [51] M. T. Neukom, S. Züfle, E. Knapp, M. Makha, R. Hany, and B. Ruhstaller, Why perovskite solar cells with high efficiency show small IV-curve hysteresis, *Sol. Energy Mater. Sol. Cells* **169**, 159 (2017).
- [52] G. Richardson, S. E. J. O’Kane, R. G. Niemann, T. A. Pelto, J. M. Foster, P. J. Cameron, and A. B. Walker, Can slow-moving ions explain hysteresis in the current-voltage curves of perovskite solar cells?, *Energy Environ. Sci.* **9**, 1476 (2016).
- [53] S. Kumar, X. Wang, J. P. Strachan, Y. Yang, and W. D. Lu, Dynamical memristors for higher-complexity neuromorphic computing, *Nat. Rev. Mater.* **7**, 575 (2022).
- [54] Z. Wang, S. Joshi, S. E. Savel’ev, H. Jiang, R. Midya, P. Lin, M. Hu, N. Ge, J. P. Strachan, Z. Li, Q. Wu, M. Barnell, G.-L. Li, H. L. Xin, R. S. Williams, Q. Xia, and J. J. Yang, Memristors with diffusive dynamics as synaptic emulators for neuromorphic computing, *Nat. Mater.* **16**, 101 (2017).
- [55] Z. S. Siwy, Ion-current rectification in nanopores and nanotubes with broken symmetry, *Adv. Funct. Mater.* **16**, 735 (2006).
- [56] B. Hille, *Ion Channels of Excitable Membranes* (Sinauer Associates, Sunderland, MA, 1992).
- [57] H. Hibino, A. Inanobe, K. Furutani, S. Murakami, I. Findlay, and Y. Kurachi, Inwardly rectifying potassium channels: their structure, function, and physiological roles, *Physiol. Rev.* **90**, 291 (2010).
- [58] A. L. Hodgkin and A. F. Huxley, A quantitative description of membrane current and its application to conduction and excitation in nerve, *J. Physiol.* **117**, 500 (1952).
- [59] T. F. Weiss, *Cellular Biophysics. Electrical Properties* (M.I.T., Cambridge, MA, 1996), Vol. 2.
- [60] D. Wang, M. Kvetny, J. Liu, W. Brown, Y. Li, and G. Wang, Transmembrane potential across single conical nanopores and resulting memristive and memcapacitive ion transport, *J. Am. Chem. Soc.* **134**, 3651 (2012).
- [61] Y. Bu, Z. Ahmed, and L. Yobas, A nanofluidic memristor based on ion concentration polarization, *Analyst* **144**, 7168 (2019).
- [62] D. Wang, W. Brown, Y. Li, M. Kvetny, J. Liu, and G. Wang, Hysteresis charges in the dynamic enrichment and depletion of ions in single conical nanopores, *ChemElectroChem* **5**, 3089 (2018).
- [63] A. Guerrero, J. Bisquert, and G. Garcia-Belmonte, Impedance spectroscopy of metal halide perovskite solar cells from the perspective of equivalent circuits, *Chem. Rev.* **121**, 14430 (2021).
- [64] A. Lasia, *Electrochemical Impedance Spectroscopy and Its Applications* (Springer, Berlin, 2014).
- [65] V. Vivier and M. E. Orazem, Impedance analysis of electrochemical systems, *Chem. Rev.* **122**, 11131 (2022).
- [66] M. W. Hirsch, S. Smale, and R. L. Devaney, *Differential Equations, Dynamical Systems, and an Introduction to Chaos*, 3rd ed. (Elsevier, Amsterdam, 2013).

- [67] M. Orlik, *Self-Organization in Electrochemical Systems I* (Springer, Berlin, 2012).
- [68] J. Bisquert, Device physics recipe to make spiking neurons, *Chem. Phys. Rev.* **4**, 031313 (2023).
- [69] J. Bisquert, Hopf bifurcations in electrochemical, neuronal, and semiconductor systems analysis by impedance spectroscopy, *Appl. Phys. Rev.* **9**, 011318 (2022).
- [70] R. Yekani, H.-c. Chiu, D. Strandell, Z. Wang, S. Bessette, R. Gauvin, P. Kambhampati, and G. P. Demopoulos, Correlation between hysteresis dynamics and inductance in hybrid perovskite solar cells: studying the dependency on ETL/perovskite interfaces, *Nanoscale* **15**, 2152 (2023).
- [71] O. Almora, I. Zarazua, E. Mas-Marza, I. Mora-Sero, J. Bisquert, and G. Garcia-Belmonte, Capacitive dark currents, hysteresis, and electrode polarization in lead halide perovskite solar cells, *J. Phys. Chem. Lett.* **6**, 1645 (2015).
- [72] N. Pellet, F. Giordano, M. I. Dar, G. Gregori, S. M. Zakeeruddin, J. Maier, and M. Grätzel, Hill climbing hysteresis of perovskite-based solar cells: A maximum power point tracking investigation, *Prog. Photovoltaics* **25**, 942 (2017).
- [73] J. Bisquert and A. Guerrero, Chemical inductor, *J. Am. Chem. Soc.* **144**, 5996 (2022).
- [74] I. Mora-Seró, J. Bisquert, F. Fabregat-Santiago, G. Garcia-Belmonte, G. Zoppi, K. Durose, Y. Y. Proskuryakov, I. Oja, A. Belaidi, T. Dittrich, R. Tena-Zaera, A. Katty, C. Lévy-Clement, V. Barrioz, and S. J. C. Irvine, Implications of the negative capacitance observed at forward bias in nanocomposite and polycrystalline solar cells, *Nano Lett.* **6**, 640 (2006).
- [75] D. Klotz, Negative capacitance or inductive loop? – A general assessment of a common low frequency impedance feature, *Electrochem. Commun.* **98**, 58 (2019).
- [76] K. Zelič, I. Mele, A. Bhowmik, and T. Kutrašnik, Phase separating electrode materials - chemical inductors?, *Energy Storage Mater.* **56**, 489 (2023).
- [77] J. Bisquert, Electrical charge coupling dominates the hysteresis effect of halide perovskite devices, *J. Phys. Chem. Lett.* **14**, 1014 (2023).
- [78] S. Ravishankar, C. Aranda, S. Sanchez, J. Bisquert, M. Saliba, and G. Garcia-Belmonte, Perovskite solar cell modeling using light and voltage modulated techniques, *J. Phys. Chem. C* **123**, 6444 (2019).
- [79] E. Ghahremanirad, A. Bou, S. Olyaei, and J. Bisquert, Inductive loop in the impedance response of perovskite solar cells explained by surface polarization model, *J. Phys. Chem. Lett.* **8**, 1402 (2017).
- [80] S.-M. Yoo, S. J. Yoon, J. A. Anta, H. J. Lee, P. P. Boix, and I. Mora-Seró, An equivalent circuit for perovskite solar cell bridging sensitized to thin film architectures, *Joule* **3**, 2535 (2019).
- [81] L. Munoz-Diaz, A. J. Rosa, A. Bou, R. S. Sanchez, B. Romero, R. A. John, M. V. Kovalenko, A. Guerrero, and J. Bisquert, Inductive and capacitive hysteresis of halide perovskite solar cells and memristors under illumination, *Front. Energy Res.* **10**, 914115 (2022).
- [82] R. S. W. Silva, F. Hartmann, and V. Lopez-Richard, The ubiquitous memristive response in solids, *IEEE Trans. Electron Devices* **69**, 5351 (2022).
- [83] R. M. Ghigliazza and P. Holmes, Minimal models of bursting neurons: How multiple currents, conductances, and timescales affect bifurcation diagrams, *SIAM J. Appl. Dyn. Syst.* **3**, 636 (2004).
- [84] C. C. Ceballos, A. C. Roque, and R. M. Leão, A negative slope conductance of the persistent sodium current prolongs subthreshold depolarizations, *Biophys. J.* **113**, 2207 (2017).
- [85] K. S. Cole and R. F. Baker, Longitudinal impedance of the squid giant axon, *J. Gen. Physiol.* **24**, 771 (1941).
- [86] K. S. Cole, *Membranes, Ions and Impulses. A Chapter of Classical Biophysics* (University of California Press, Berkeley, CA, 1968).
- [87] K. S. Cole, Rectification and inductance in the squid giant axon, *J. Gen. Physiol.* **25**, 29 (1941).
- [88] D. A. Jacobs, H. Shen, F. Pfeffer, J. Peng, T. P. White, F. J. Beck, and K. R. Catchpole, The two faces of capacitance: New interpretations for electrical impedance measurements of perovskite solar cells and their relation to hysteresis, *J. Appl. Phys.* **124**, 225702 (2018).
- [89] F. Ebadi, N. Taghavinia, R. Mohammadpour, A. Hagfeldt, and W. Tress, Origin of apparent light-enhanced and negative capacitance in perovskite solar cells, *Nat. Commun.* **10**, 1574 (2019).
- [90] J. Bisquert, Negative inductor effects in nonlinear two-dimensional systems. Oscillatory neurons and memristors, *Chem. Phys. Rev.* **3**, 041305 (2022).
- [91] F. Wu, R. Pathak, K. Chen, G. Wang, B. Bahrami, W.-H. Zhang, and Q. Qiao, Inverted current–voltage hysteresis in perovskite solar cells, *ACS Energy Lett.* **3**, 2457 (2018).
- [92] N. E. Courtier, J. M. Cave, J. M. Foster, A. B. Walker, and G. Richardson, How transport layer properties affect perovskite solar cell performance: Insights from a coupled charge transport/ion migration model, *Energy Environ. Sci.* **12**, 396 (2019).
- [93] M. Koch, H. Tseng, A. Weissbach, B. Iniguez, K. Leo, A. Kloes, H. Kleemann, and G. Darbandy, Device physics, modeling and simulation of organic electrochemical transistors, *IEEE J. Electron Devices Soc.* **11**, 665 (2023).
- [94] R. Waser and M. Aono, Nanoionics-based resistive switching memories, *Nat. Mater.* **6**, 833 (2007).
- [95] J. Bisquert, Current-controlled memristors: Resistive switching systems with negative capacitance and inverted hysteresis, *Phys. Rev. Appl.* **20**, 044022 (2023).
- [96] C. Gonzales, A. Guerrero, and J. Bisquert, Spectral properties of the dynamic state transition in metal halide perovskite-based memristor exhibiting negative capacitance, *App. Phys. Lett.* **118**, 073501 (2021).
- [97] P. Ramirez, J. Cervera, S. Nasir, M. Ali, W. Ensinger, and S. Mafé, Electrochemical impedance spectroscopy of membranes with nanofluidic conical pores, *J. Colloid Interface Sci.* **655**, 876 (2024).
- [98] J. Cervera, B. Schiedt, R. Neumann, S. Mafé, and P. Ramirez, Ionic conduction, rectification, and selectivity in single conical nanopores, *J. Chem. Phys.* **124**, 104706 (2006).
- [99] P. Gkoupidenis, N. Schaefer, B. Garlan, and G. G. Malliaras, Neuromorphic functions in PEDOT:PSS organic electrochemical transistors, *Adv. Mater.* **27**, 7176 (2015).

- [100] P. C. Harikesh, C.-Y. Yang, H.-Y. Wu, S. Zhang, M. J. Donahue, A. S. Caravaca, J.-D. Huang, P. S. Olofsson, M. Berggren, D. Tu, and S. Fabiano, Ion-tunable antiambipolarity in mixed ion–electron conducting polymers enables biorealistic organic electrochemical neurons, *Nat. Mater.* **22**, 242 (2023).
- [101] P. C. Harikesh, C.-Y. Yang, D. Tu, J. Y. Gerasimov, A. M. Dar, A. Armada-Moreira, M. Massetti, R. Kroon, D. Bliman, R. Olsson, E. Stavrinidou, M. Berggren, and S. Fabiano, Organic electrochemical neurons and synapses with ion mediated spiking, *Nat. Commun.* **13**, 901 (2022).
- [102] G. Lanzani, Organic electronics meets biology, *Nat. Mater.* **13**, 775 (2014).
- [103] B. D. Paulsen, K. Tybrandt, E. Stavrinidou, and J. Rivnay, Organic mixed ionic–electronic conductors, *Nat. Mater.* **19**, 13 (2020).
- [104] J. Bisquert, Hysteresis in organic electrochemical transistors: Distinction of capacitive and inductive effects, *J. Phys. Chem. Lett.* **14**, 10951 (2023).
- [105] D. Ohayon, V. Druet, and S. Inal, A guide for the characterization of organic electrochemical transistors and channel materials, *Chem. Soc. Rev.* **52**, 1001 (2023).
- [106] A. Weissbach, L. M. Bongartz, M. Cucchi, H. Tseng, K. Leo, and H. Kleemann, Photopatternable solid electrolyte for integrable organic electrochemical transistors: Operation and hysteresis, *J. Mater. Chem. C* **10**, 2656 (2022).
- [107] V. Kaphle, S. Liu, C.-M. Keum, and B. Lüssem, Organic electrochemical transistors based on room temperature ionic liquids: Performance and stability, *Phys. Status Solidi A* **215**, 1800631 (2018).
- [108] D. A. Bernards and G. G. Malliaras, Steady-state and transient behavior of organic electrochemical transistors, *Adv. Funct. Mater.* **17**, 3538 (2007).
- [109] L. Gracia, J. García-Cañadas, G. Garcia-Belmonte, A. Beltrán, J. Andrés, and J. Bisquert, Composition dependence of the energy barrier for lithium diffusion in WO_3 , *Electrochem. Solid State Lett.* **8**, J21 (2005).
- [110] J. Bisquert, Physical electrochemistry of nanostructured devices, *Phys. Chem. Chem. Phys.* **10**, 49 (2008).
- [111] E. Hernandez-Balaguera and J. Bisquert, Time transients with inductive loop traces in metal halide perovskites, *Adv. Funct. Mater.* (2023).
- [112] P. Ramirez, A. Bou, J. Cervera, and J. Bisquert, Inductive nanopore synapse element for iontronic neuromorphic computing, *Res. Square* (2023).
- [113] V. M. Le Corre, J. Diekmann, F. Peña-Camargo, J. Thiesbrummel, N. Tokmoldin, E. Gutierrez-Partida, K. P. Peters, L. Perdigón-Toro, M. H. Futscher, F. Lang, J. Warby, H. J. Snaith, D. Neher, and M. Stollerfoht, Quantification of efficiency losses due to mobile ions in perovskite solar cells via fast hysteresis measurements, *Sol. RRL* **6**, 2100772 (2022).
- [114] J. Wu, Y. Li, Y. Li, W. Xie, J. Shi, D. Li, S. Cheng, and Q. Meng, Using hysteresis to predict the charge recombination properties of perovskite solar cells, *J. Mater. Chem. A* **9**, 6382 (2021).
- [115] N. E. Courtier, J. M. Cave, A. B. Walker, G. Richardson, and J. M. Foster, IonMonger: A free and fast planar perovskite solar cell simulator with coupled ion vacancy and charge carrier dynamics, *J. Comput. Electron.* **18**, 1435 (2019).
- [116] B. Muthuswamy, J. Jevtic, H. H. C. Iu, C. K. Subramaniam, K. Ganesan, V. Sankaranarayanan, K. Sethupathi, H. Kim, M. P. Shah, and L. O. Chua, in *2014 IEEE International Symposium on Circuits and Systems (ISCAS)* (2014).
- [117] M. D. Pickett, D. B. Strukov, J. L. Borghetti, J. J. Yang, G. S. Snider, D. R. Stewart, and R. S. Williams, Switching dynamics in titanium dioxide memristive devices, *J. Appl. Phys.* **106**, 074508 (2009).
- [118] J. Diekmann, F. Peña-Camargo, N. Tokmoldin, J. Thiesbrummel, J. Warby, E. Gutierrez-Partida, S. Shah, D. Neher, and M. Stollerfoht, Determination of mobile ion densities in halide perovskites via low-frequency capacitance and charge extraction techniques, *J. Phys. Chem. Lett.* **14**, 4200 (2023).
- [119] M. Taukeer Khan, F. Khan, A. Al-Ahmed, S. Ahmad, and F. Al-Sulaiman, Evaluating the capacitive response in metal halide perovskite solar cells, *Chem. Rec.* **n/a**, e202100330 (2022).
- [120] G. A. Sepalage, S. Meyer, A. Pascoe, A. D. Scully, F. Huang, U. Bach, Y.-B. Cheng, and L. Spiccia, Copper(I) iodide as hole-conductor in planar perovskite solar cells: Probing the origin of J–V hysteresis, *Adv. Funct. Mater.* **25**, 5650 (2015).
- [121] J. Bisquert, A. Bou, A. Guerrero, and E. Hernández-Balaguera, Resistance transient dynamics in switchable perovskite memristors, *APL Mach. Learn.* **1**, 036101 (2023).
- [122] E. Hernández-Balaguera, L. Muñoz-Díaz, A. Bou, B. Romero, B. Ilyassov, A. Guerrero, and J. Bisquert, Long-term potentiation mechanism of biological postsynaptic activity in neuro-inspired halide perovskite memristors, *Neuromorphic Comput. Eng.* **3**, 024005 (2023).
- [123] J. Bisquert, Iontronic Nanopore model for artificial neurons: The requisites of spiking, *J. Phys. Chem. Lett.* **14**, 9027 (2023).
- [124] E. Ghahremanirad, O. Almora, S. Suresh, A. A. Drew, T. H. Chowdhury, and A. R. Uhl, Beyond protocols: Understanding the electrical behavior of perovskite solar cells by impedance spectroscopy, *Adv. Energy Mater.* **13**, 2204370 (2023).